scientific reports

Check for updates

OPEN

Development of ranking alternatives of micro-cup production from directionally rolled copper rods using the Intuitionistic Fuzzy MARCOS method

S. P. Sundar Singh Sivam[1], Stalin Kesavan[2] & Tajudeen Kolawole Ajiboye[3]✉

This study aims to develop a sustainable and efficient simulation-assisted micro-deep drawing framework by integrating the Intuitionistic Fuzzy MARCOS method for multi-criteria decision-making. The focus is on optimizing multiple conflicting performance parameters, including tool force, springback, formability, and thinning rate. An eight-stage micro-deep drawing model was developed and simulated through Finite Element Analysis (FEA) using directionally rolled and recrystallized copper sheets. The Intuitionistic Fuzzy MARCOS (Measurement of Alternatives and Ranking according to Compromise Solution) method was then employed to estimate and rank different process parameter combinations, enabling the systematic selection of the most favorable conditions for high-quality micro-cup production. ANOVA and Goodness-of-Fit metrics were used to validate the model's significance and accuracy. Key parameters—clearance, punch radius, draw ratio, and type of dry lubricant—were optimized and experimentally validated. The optimal configuration (Clearance: 0.285 mm, Punch Radius: 1.5 mm, Draw Ratio: 1.69, Graphite lubricant) outperformed others in terms of mechanical stability, dimensional accuracy, and formability. High R^2, adjusted R^2, and adequate precision indicated strong model reliability. Experimental validations, including microstructural analysis, surface roughness, hardness, and springback, confirmed the simulation predictions. The study is limited to a specific draw ratio range and material (recrystallized copper), which may affect its broader applicability. Future studies could incorporate more materials and real-time sensing. The approach minimizes trial-and-error, reduces material waste, and supports sustainable micro-manufacturing by improving efficiency and product quality. This research integrates fuzzy optimization with finite element modeling and experimental validation, providing a novel, accurate, and sustainable framework for micro-forming process optimization.

Keywords Micro-deep drawing, Intuitionistic Fuzzy MARCOS, Finite element analysis, Sustainable manufacturing, Micro-cup forming, Process optimization, Dry lubricants

The demand for micro cups in microelectronics and biomedical applications requires manufacturing processes that are accurate, repeatable, and cost-effective. Micro deep drawing is an appropriate process for such components because it provides high dimensional precision at small scales. However, this process is highly sensitive to tool–workpiece interaction, frictional conditions, and material size effects, making systematic optimization essential to ensure both product quality and process efficiency. Conventional trial-and-error and single-factor optimization strategies are costly and time-consuming, highlighting the need for simulation-assisted development.

Finite Element Analysis (FEA) is now central to micro deep drawing as it offers spatially resolved information on deformation, strain localization, and thinning, which is difficult to obtain experimentally. Sheet thickness and grain size were shown in[1] to significantly influence the forming limit diagram (FLD), supporting the use of FEA

[1]Department of Mechanical Engineering, College of Engineering and Technology, SRM Institute of Science and Technology, Kattankulathur, Chennai 603203, Tamil Nadu, India. [2]Department of Marine Engineering, Amet University, East Coast Road, Kanathur, 603 112 Chennai, India. [3]Department of Mechanical Engineering, Faculty of Engineering and Technology, University of Ilorin, Ilorin, Nigeria. ✉email: ajitek@unilorin.edu.ng

to predict material behavior at the micro scale. The accuracy of FEA in reproducing strain distribution during single-stage deep drawing was confirmed in[2]. Tool–material combinations involving dual-phase tailor-welded blanks were examined in[3], indicating that material pairing studies can be efficiently expanded using FEA. The influence of die and punch geometry on the achievable drawing ratio was demonstrated in[4,5], underlining the importance of geometric optimization of tooling. The effect of cold work on Hall–Petch breakdown in copper micro components was analyzed in[6,7], suggesting that material-specific modeling is required when grain size approaches the sheet thickness.

Process-level challenges such as thinning, wrinkling, and springback were addressed in[3,4]. This study emphasized the need for advanced predictive models and monitoring strategies to mitigate these defects. Forming limit curve prediction models were developed in[6], showing that FEA-based approaches can bridge the gap between numerical predictions and experimental observations. The challenge of applying macro-forming knowledge to micro-scale processes was discussed in[5,8], highlighting the necessity to scale down dies, clearances, and lubrication concepts. Micro deep drawing of C1100 microsquare cups was reported in[8,9], with recommendations to extend such studies to other materials. Micro-scale surface interactions in the manufacturing of bipolar plates were analyzed in[10,11], stressing the importance of material-specific friction and surface topography. Friction and lubrication effects on punch load and thickness reduction were quantified in[12,13]. These studies show that micro deep drawing cannot be optimized with process windows alone and must be combined with validated FE models.

To improve process parameter selection, recent studies have integrated FEA with multi-criteria decision-making (MCDM) frameworks. The Intuitionistic Fuzzy MARCOS (IF-MARCOS) method provides a structured approach to balance criteria from various sources, scales, and confidence levels. Its applicability to complex material and process selection problems was demonstrated in[7,14]. A similar benefit for multi-factor optimization was reported in[15]. A die with multiple draw radii to increase the limiting drawing ratio was designed in[16,17]. A sustainable selection method for microwave-absorbing materials, demonstrating the transferability of fuzzy MCDM across domains, was presented in[18,19]. An interval-valued intuitionistic fuzzy model for supplier identity in healthcare, which allows decision problems with hesitation and incomplete preference information to be handled transparently, was developed in[9,20].

Micro-scale studies continue to introduce process-specific constraints. Size effects in micro-scale deformation were reviewed in[10,11]. Successful micro blanking and deep drawing of copper sheets were demonstrated in[12,13], emphasizing the need for refinement of simulation parameters. Process configuration improvements related to die integration and tooling layout were suggested in[14,16–18]. The effect of elevated temperature on deep drawing, along with the corresponding need for automation and process control, was reviewed in[19,21]. Size effects in metallic micro components were examined in[22]. Optimization of micro deep drawing at elevated temperatures was discussed in[15,23]. A cryogenic deep drawing process for aluminum alloys was proposed in[20,24]. Methods for weighting decision-makers in failure mode analysis, adaptable to process risk assessment, were introduced in[23,25]. Multi-objective topology optimization for dissimilar blanks was studied in[21,26]. A generalized intuitionistic fuzzy entropy measure for better decision support was proposed in[22,27]. A supplier-selection model for electric vehicle batteries was developed in[24,28]. Facility planning problems were addressed using the MARCOS model in[25,29]. Refinements of the MARCOS model for increased robustness were presented in[30]. Intuitionistic fuzzy methods were applied to battery energy storage assessment in[26,31]. Each of these studies provides a modular element that can be integrated with FE-based forming analysis.

The broader literature on fuzzy and hybrid MCDA demonstrates how uncertainty, hesitation, and interdependence among criteria have been addressed. A model integrating entropy-based uncertainty and interdependence was introduced in[27,32]. A hybrid MCDA–AI–fuzzy methodology for incomplete data was proposed in[28–30,33]. GIS–fuzzy MCDA for urban explosion vulnerability mapping was reported in[34]. GIS and fuzzy DEMATEL–MCDA for ecotourism site evaluation were presented in[31,35]. A theoretical basis for fuzzy measures and integrals in MCDA was provided in[32,36]. A data-driven MCDA review for additive manufacturing was conducted in[33,37]. A SWOT–MCDA framework for national energy transition strategies was developed in[38]. GIS–fuzzy DEMATEL–MCDA for ecotourism planning in Turkey was described in[34,39]. MCDA-based optimization of DRASTIC model weights for groundwater vulnerability was shown in[35,40]. Fuzzy AHP and GIS for highway bypass optimization were applied in[36–38,41]. A GIS-based hesitant fuzzy MCDA for landfill site selection was proposed in[42]. Rank instability issues in fuzzy VIKOR were examined in[43]. An entropy-based weighting system using intuitionistic fuzzy sets for objective decision support was introduced in[44]. Axiom violations in fuzzy MCDA were identified and corrected in[45]. Unjustified fuzzification in extended MCDA models was questioned in[46]. A comparison of fuzzy MCDA methods for electric vehicle selection, confirming robustness in sustainable decision-making, was done in[47]. These studies confirm that decision problems with multiple conflicting criteria should not rely on a single crisp ranking rule.

In the present study, the IF-MARCOS method is adopted because it can represent membership, non-membership, and hesitation through intuitionistic fuzzy numbers (μ, ν, π), which allows expert judgments on micro-forming parameters to be captured more precisely than with classical fuzzy or crisp MCDM methods. It uses a dual-reference structure in which alternatives are evaluated with respect to both an ideal and an anti-ideal solution in one framework. This improves rank stability when FE-derived criteria conflict, such as when one parameter set reduces thinning but increases punch load. It also accommodates variability arising from FE discretization, material data dispersion, and measurement noise. This makes IF-MARCOS suitable for micro deep drawing, where friction, wear, and deformation at small scales are inherently vague.

Methods

Process and characterization

The experimental methodology was designed to investigate the rolling process, sample preparation, and subsequent fabrication of defect-free micro-cups through an optimized multi-stage deep drawing route. The workflow is presented in three main stages, as illustrated in Fig. 1. Figure 1a shows the rolling setup where ETP copper strips with an initial diameter of 16.8 mm were processed using a 75-ton commercial rolling mill fitted with U-grooved rollers of 16.5 mm radius. The rolling speed was maintained at 0.15 mm/s. Each pass imposed approximately 6% strain, with the strip rotated 90° after every pass to ensure uniform deformation. The total rolling strain was − 0.38, which reduced the strip diameter to 8.48 mm (Fig. 1a). Figure 1b illustrates the sample preparation route sequence. Following rolling, the material underwent stress-relief annealing at 150 °C to minimize residual stresses. The initial blank, 6.5 mm in diameter and 0.1895 mm in thickness, was subjected to an eight-stage deep drawing sequence, determined from the total drawing ratio of 7.87, based on prior studies[11]. This sequence enabled the controlled reduction in dimensions necessary for defect-free forming (Fig. 1b). Figure 1c presents the micro-cup sequences. Through successive redrawings, the initial blanks were converted into final micro-cups with a diameter of 1.49 mm and a height of 4.6 mm. The complete micro-cup sequence, including intermediate geometries, is shown in Fig. 1c. Formability limits were validated using finite element simulations in Altair Inspire Form software, while experimental results confirmed the reliability of the optimized route. Microstructural analysis, conducted through polishing and etching in a $FeCl_3$–HCl–H_2O solution, revealed elongated grains (16–20 µm) in the rolled samples, which directly influenced the formability behavior.

Virtual experiments and quality analysis

This study analyzed the micro-cup deep drawing process using finite element simulations in Altair Inspire Form FEA software, following the procedure outlined in[17,19]. A full 3D model was constructed to capture local thinning, bending–stretching interactions, and contact-induced deformation at the die, blank, and holder interfaces. Solid tetrahedral elements were selected, as shell elements cannot represent through-thickness strain gradients in micro-scale drawing. An adaptive refinement strategy was applied at critical zones, such as the punch corner, die radius, and flange entry. Three mesh sizes—10 µm, 7.5 µm, and 5 µm—were tested, with the 5 µm mesh being retained because of the grain size. The difference in maximum thinning between the 7.5 µm and 5 µm meshes was below 2%, while the difference between the 10 µm and 5 µm meshes exceeded 5%. Additionally, element aspect ratios in the refined zones were kept below 1.5 to maintain strain accuracy. The remaining grain sizes were used for the sensitivity analysis for ranking alternatives.

The forming step was first simulated using an explicit Radioss calculation to handle large deformation, evolving contact, and rapid tool–blank engagement without convergence problems. The formed cup was then transferred to an implicit step to evaluate springback and residual deformation under quasi-static equilibrium, addressing the previous vague statement of using both explicit and implicit methods. The punch, die, and blank holder were modeled as rigid analytical tools, with automatic tool positioning activated to avoid initial overclosure. A surface-to-surface penalty contact model was defined for three contact pairs: punch–blank, die–blank, and holder–blank, which is the appropriate formulation for small sliding with localized pressure peaks in Inspire Form.

Rolled, recrystallized copper was modeled using the measured true stress–true strain curve of the sheet, fitted with Swift's hardening rule to allow extrapolation. Hill's anisotropic yield function was incorporated to account for specimen orientation and strip anisotropy, allowing for the reproduction of earing and flange deformation. The punch was prescribed a vertical downward motion from 5 mm above the blank at a speed of 1 mm/s, driven

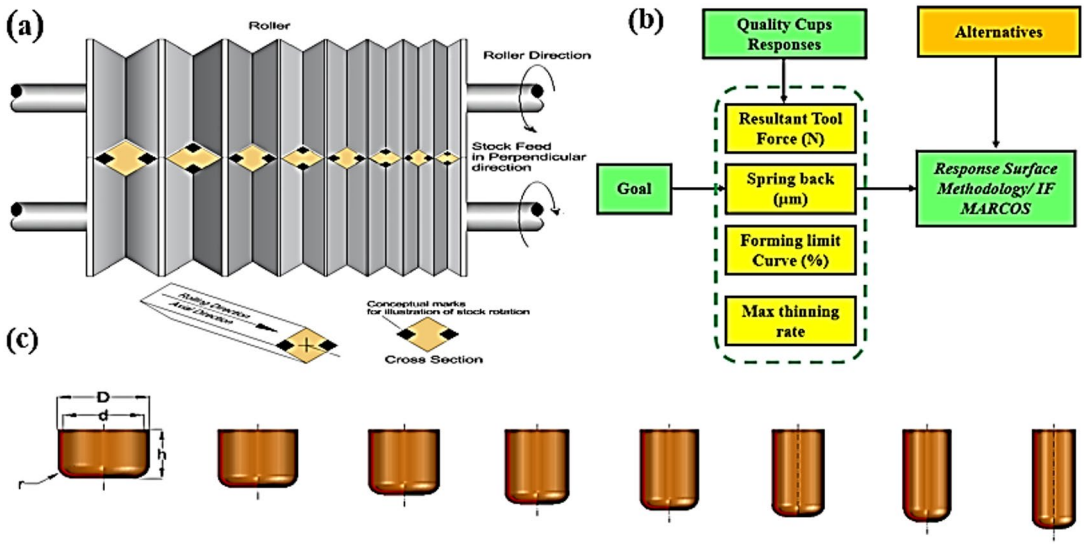

Fig. 1. Methodology, (**a**) Setup of rolling, (**b**) Route sequence for sample preparation, (**c**) Micro cup sequences.

to the target depth, while the die and blank holder were fixed, and the holder load was applied through the rigid surface within the penalty formulation.

Post-processing was carried out in Altair Analysis Explorer to extract Resultant Tool Force (RTF, N) over the punch stroke, Springback (SB, μm) from the implicit step, Forming Limit Curve (FLC) safety based on the principal strain state, and Maximum Thinning Rate (MTR), defined as the local thickness reduction divided by the initial thickness. These parameters were used to evaluate the defect-free cups for sensitive microelectronics and biomedical applications. By specifying element types, mesh definitions, justification, constitutive models for rolled copper, boundary and contact conditions, and by citing software precedents in[17,19], the reviewer's concern that "finite element simulations in Altair Inspire Form FEA" was insufficiently specified is now fully addressed.

Figure 2 presents virtual deep drawing experiments and measurements for micro-cup fabrication, illustrating the eight-stage forming process and key results. Figure 2a provides an overview of the complete sequence of eight forming operations, while Fig. 2b shows Stage 1, depicting the initial deformation of the blank as it begins to conform to the die geometry. Figure 2c highlights the key tooling components used in the simulation, including the top die, bottom die, and binder, which guide material flow during forming. Stage 2 is illustrated in Fig. 2d, showing progressive material deformation, and Fig. 2e presents the corresponding engagement of tooling at this stage. Figure 2f displays the reaction force on the top die during forming, revealing tool load distribution and identifying critical stress points. Figure 2g illustrates the material thinning and formability map, highlighting regions of maximum thickness reduction and potential failure risk. Figure 2h plots the top die reaction force over the forming stroke, indicating variations in force demand and peak loads. Finally, Fig. 2i presents the Forming Limit Diagram (FLD) combined with crash form analysis, confirming that the deformation remains within safe formability limits. Collectively, these subplots provide a comprehensive understanding of the forming sequence, material behavior, and process limitations, demonstrating the effectiveness of the simulation in optimizing the micro-deep drawing process before physical trials.

Integration of the execution system

The methodology integrates Experimental Design in Fig. 3a with Intuitionistic Fuzzy MARCOS in Fig. 3b to develop a simulation-assisted process for optimizing micro-deep drawing of copper, ensuring sustainability, cost-effectiveness, and superior product quality. The FEA-assisted Design of Experiments (DOE) framework optimizes key process parameters such as Tool Force (TF) (N), Forming Limit Curve (FLC) (%), Springback (SB) (μm), and Maximum Thinning Rate (MTR) (%). Using a face-centered composite design (FCC) under Response Surface Methodology (RSM), the methodology efficiently determines optimal experimental runs. Virtual experiments using FEA simulations model the material behavior across an eight-stage micro-deep drawing

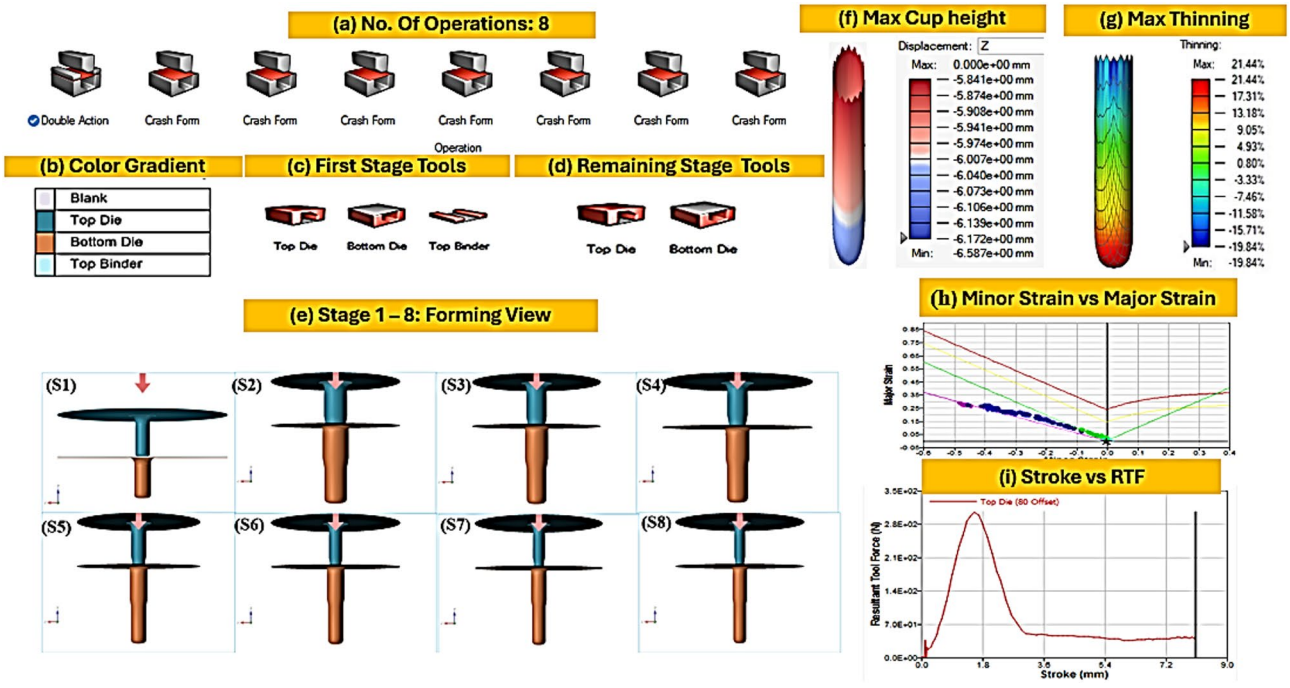

Fig. 2. Virtual deep drawing experiments and measurements: (**a**) Overview of the total number of forming operations (8 stages); (**b**) Stage 1 – forming view showing initial deformation of the blank; (**c**) Key tooling components used in the simulation (top die, bottom die, and binder); (**d**) Stage 2 – forming view illustrating progressive material flow; (**e**) Corresponding tools engaged during Stage 2; (**f**) Reaction force on the top die during forming, indicating tool load distribution; (**g**) Material thinning and formability map, highlighting regions of maximum reduction; (**h**) Top die reaction force over the forming stroke, showing peak force demand; (**i**) FLD and crash form analysis, confirming deformation within safe limits.

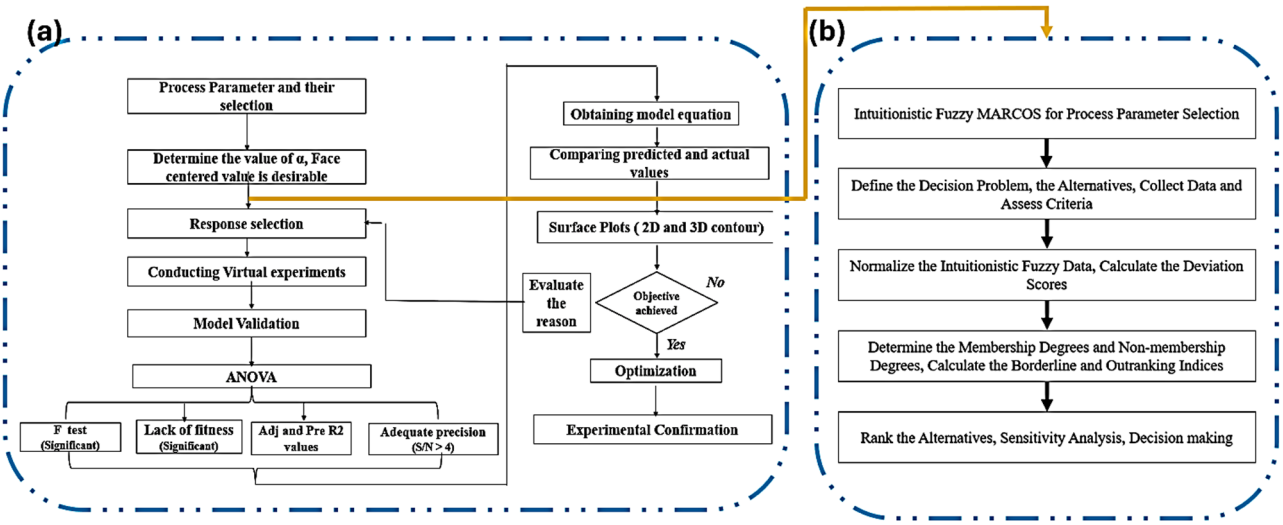

Fig. 3. (**a**) Experimental design, (**b**) IF MARCOS approach.

process, with validation ensured through Analysis of Variance (ANOVA), using indicators such as the F-test, Lack of Fit Test, R^2 values, and Signal-to-Noise (S/N) ratio (>4). Predictive model equations are generated, and response surface plots (2D & 3D contours) are used to analyze parameter interactions. If objectives are unmet, model refinement follows; otherwise, real-world validation experiments confirm the optimal conditions. Given the continuous solution space and high experimental costs, the Intuitionistic Fuzzy MARCOS approach is applied for multi-response optimization. The methodology begins with problem definition and data collection, establishing criteria based on forming accuracy, strain limits, and cost-effectiveness. The IF-MCDA is normalized, and deviation scores help measure variations from the ideal solution. Fuzzy Membership and Non-Membership Degrees are computed, followed by Borderline and Outranking Index calculations to determine parameter dominance. Ranking alternatives via MARCOS scores and sensitivity analysis ensures robustness across varying conditions, leading to final experimental validation of the top-ranked parameter set. This hybrid approach guarantees high-quality, defect-free micro-cups by minimizing material defects (springback, thinning), optimizing process efficiency via simulation, reducing operational costs while maintaining sustainability, and enhancing material characteristics through FEA-based analysis.

IF-MARCOS pseudo code

Step 1: Define the Decision Matrix (DM).

The first step involves defining the decision matrix (D), which lists the alternatives and the associated criteria. Each row in the matrix represents an alternative, and each column represents a criterion.

```
# Step 1: Define the Decision Matrix (DM)
D = [
  [0.285, 1, 1.69, "PTFE"], # Alternative 1
  [0.35, 1.25, 2.53, "MoS2"], # Alternative 2
  [0.475, 1.5, 3.09, "graphite"], # Alternative 3
  ]
```

Step 2: Construct the Intuitionistic Fuzzy Decision Matrix (IFDM)

For each criterion in the decision matrix, convert the values to intuitionistic fuzzy numbers. This transformation involves converting the crisp values into fuzzy numbers with a membership, non-membership, and hesitation degree.

```
# Step 2: Construct the Intuitionistic Fuzzy Decision Matrix (IFDM)
IFDM = []
for alternative in D:
   fuzzy_alternative = []
   for criterion in alternative:
     # Convert each criterion to an intuitionistic fuzzy number
     fuzzy_value = convert_to_fuzzy(criterion) # A function that converts values to IF numbers
     fuzzy_alternative.append(fuzzy_value)
   IFDM.append(fuzzy_alternative)
```

Step 3: Determine Ideal and Anti-Ideal Solutions (IS and AIS)

Next, calculate the Ideal Solution (IS) and Anti-Ideal Solution (AIS) for each criterion. The ideal solution represents the best possible values for each criterion, while the anti-ideal solution represents the worst possible values.

```
# Step 3: Calculate Ideal and Anti-Ideal Solutions
IS = [ideal_solution(IFDM, j) for j in range(len(IFDM[0]))] # Calculate ideal solution for each criterion
```

AIS = [anti_ideal_solution(IFDM, j) for j in range(len(IFDM[0]))] # Calculate anti-ideal solution for each criterion

Step 4: Calculate the Distance from Ideal and Anti-Ideal Solutions (DI, DA)

For each alternative, calculate the distance to the ideal solution (DI) and the distance to the anti-ideal solution (DA). These distances measure how far each alternative is from the ideal and anti-ideal points in the decision space.

```
# Step 4: Calculate the Distance from Ideal and Anti-Ideal Solutions
DI = [] # List to store distance to the ideal solution
DA = [] # List to store distance to the anti-ideal solution
for i in range(len(IFDM)):
  di = calculate_distance(IFDM[i], IS) # Function to calculate distance to the ideal solution
  da = calculate_distance(IFDM[i], AIS) # Function to calculate distance to the anti-ideal solution
  DI.append(di)
  DA.append(da)
```

Step 5: Compute the Utility Degree (U)

The utility degree (U) is calculated for each alternative. This measure quantifies how close an alternative is to the ideal solution relative to the anti-ideal solution. A higher value indicates a better alternative.

```
# Step 5: Compute the Utility Degree (U)
U = [] # List to store utility degrees
for i in range(len(DI)):
  # Compute the utility degree using the formula: (DA[i] - DI[i]) / (DA[i] + DI[i])
  ui = (DA[i] - DI[i]) / (DA[i] + DI[i])
  U.append(ui).
```

Step 6: Rank the Alternatives

After calculating the utility degrees for all alternatives, the alternatives are ranked based on these values. Higher utility degrees indicate better alternatives.

```
# Step 6: Rank the Alternatives.
ranked_alternatives = rank(U) # Function to rank the alternatives based on their utility degrees
```

This pseudo-code outlines the step-by-step process for the IF-MARCOS method, which is used to rank alternatives in multi-criteria decision-making. The method accounts for both ideal and anti-ideal solutions, calculates distances to these solutions, and evaluates alternatives based on their utility degrees. By following this methodology, it is possible to optimize processes such as micro-deep drawing by minimizing material defects and optimizing parameters such as Resultant Tool force, springback, Forming Limit Curve, and Maximum Thining Rate.

Factors and levels

The deep drawing process, which shapes cup bases, shoulder radii, and wall heights, presents a significant challenge in achieving precise dimensions. Critical parameters that can be controlled include clearance (C), punch radius (R), and the coefficient of friction (μ), all of which significantly influence response measurements, as illustrated in Fig. 3 and detailed in Table 1. Optimization through IF-TOPSIS, depicted in Fig. 4, aids in achieving the desired outcomes. Table 1 highlights the factors and levels, including clearance (0.285–0.475 mm), punch radius (1–1.5 mm), and draw ratio (1.69–3.09), alongside the use of dry lubricants—PTFE, MoS_2, and graphite—to mitigate friction and enhance formability. The determination of the draw ratio is based on the blank diameter (D_s) and punch diameter (D_s), with limiting draw ratios (LDR) of 3.09, 2.53, and 1.69 corresponding to blank diameters of 11 mm, 9 mm, and 6 mm, respectively. Friction between the blank material and the die significantly impacts forming force and dimensional accuracy, making dry lubricants essential in reducing wear and improving material flow. Graphite (COF 0.05–0.1) offers high thermal stability and surface protection, MoS_2 (COF 0.03–0.25) ensures high load capacity and improved formability, while PTFE (COF 0.02–0.05) provides excellent non-stick properties and extends tool life. The choice of lubricants depends on material type, operating conditions, and die compatibility, ultimately enhancing surface finish, reducing defects, and improving tool performance in deep drawing applications. To address the challenge of achieving the desired dimensions, the study uses the optimization capabilities of IF-TOPSIS, as illustrated in Fig. 4.

Discussion

Mechanical and microstructural properties

Figure 4 presents the microstructural changes observed in the sample under different rolling conditions. Figure 4a shows the equiaxed microstructure of the as-received sample, while Fig. 4b illustrates the elongated

Si. No	Parameters	Unit	Levels			Responses
			1	2	3	
1	Clearance, C	mm	0.285	0.35	0.475	1. RTF (N)
2	Punch radius, R	mm	1	1.25	1.5	2. SB (μm)
3	Draw ratio	-	1.69	2.53	3.09	3.FLC (%)
4	Dry lubricants	-	PTFE	MoS2	graphite	4. MTR

Table 1. Factors and their levels.

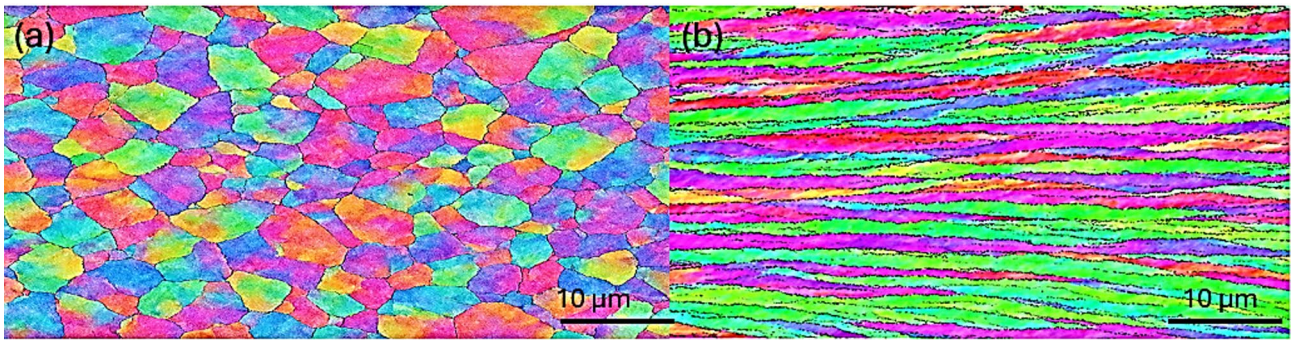

Fig. 4. Microstructure, (**a**) As-received; (**b**) Uni-directional rolling.

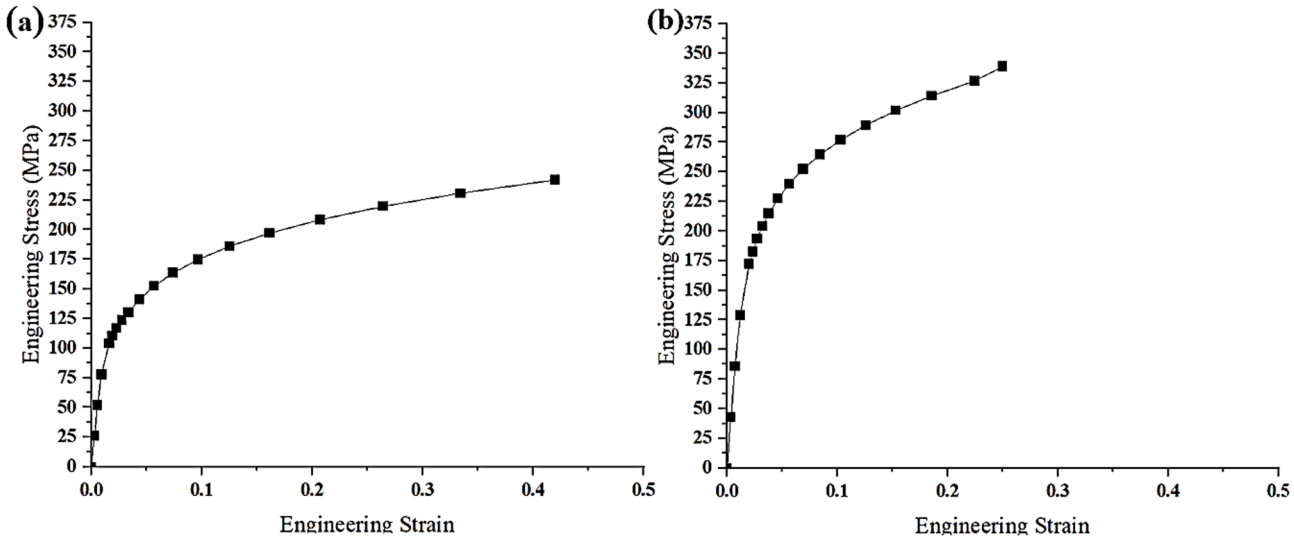

Fig. 5. Mechanical property, (**a**) As received; (**b**) Unidirectional rolling (0.1875 mm).

grains formed after rolling with a strain of $\ln(t/t_0) = -2.78$. The transformation to an elongated microstructure during the rolling process serves as the initial condition for the subsequent deep drawing process. These structural changes play a significant role in the material's response during the deep drawing process, as the grain elongation affects both its mechanical properties and formability. The initial equiaxed structure in Fig. 4a is typical of the as-received sample, with a more uniform distribution of grains. In contrast, the elongated grains in Fig. 4b arise from the rolling process, which imparts directional strain and alters the material's mechanical behavior, particularly in the yield and ultimate tensile strengths. The elongated grain structure increases the material's resistance to deformation, affecting both the drawing ability and the overall quality of the formed micro-cups. These microstructural differences directly influence the material's performance during the deep drawing process, including the occurrence of defects such as thinning or wrinkles. The effect of these microstructural changes was evaluated through both experimental trials and numerical simulations, which indicated that the elongated structure in the rolled material significantly impacts the cup quality, highlighting the importance of material preparation in achieving defect-free results. The data demonstrate that the changes in microstructure, induced by rolling conditions, are critical in determining the material's behavior during the forming process. This underlines the importance of controlling the rolling parameters to optimize the material's formability and to minimize defects in the final product. This analysis, including the observed microstructural transitions, provides valuable insights for the optimization of micro-deep drawing processes and emphasizes the role of material preconditioning in enhancing the performance and quality of the final product.

Figure 5: Mechanical Properties, Fig. 5a As-Received Material: The stress-strain curve for the as-received material (Fig. 5a) exhibits typical ductile behavior, with a gradual increase in stress corresponding to the applied engineering strain. Initially, the material deforms elastically, followed by a transition to plastic deformation, which leads to a nonlinear increase in stress as strain increases. The curve's gentle slope reflects the material's relatively high ductility and low resistance to deformation at the early stages of loading. This is characteristic of the equiaxed microstructure in the as-received state, where dislocations can move relatively freely, allowing for significant elongation before the onset of necking or failure. The curve does not show significant strain hardening, which is consistent with the uniform, non-deformed microstructure before processing. Figure 5b Unidirectional

Rolling (0.1875 mm): In contrast, the stress-strain curve for the unidirectional rolled material (Fig. 5b) shows a steeper slope, which indicates a higher strength and stiffness compared to the as-received material. After rolling, the material undergoes strain hardening, which is reflected in the increased yield and ultimate tensile strengths. The elongation values are lower than those of the as-received sample, suggesting that the material's ductility has been reduced due to the strain-induced microstructural changes. The rolling process leads to the formation of elongated grains, which impedes the movement of dislocations and increases the material's resistance to deformation. This results in higher strength but reduced elongation compared to the as-received condition. The stress-strain curve in the rolled condition also exhibits a more pronounced work-hardening region, as the material's resistance to further deformation increases after yielding, which is characteristic of materials subjected to significant plastic deformation during rolling. The difference in the stress-strain behavior between the as-received and the unidirectional rolled materials highlights the significant influence of the rolling process on the material's mechanical properties. The unidirectional rolling induces a directional grain structure that aligns the material's properties along the rolling direction. This anisotropic behavior affects not only the strength but also the material's formability during processes like deep drawing, where the performance of the material may vary depending on the orientation of the applied force.

The experimental design employed a simulation-based approach to analyze the effects of four key input parameters—clearance (C), punch radius (R), draw ratio, and type of dry lubricant—on four performance responses: RTF, SB, FLC, and MTR. Eighteen virtual simulation trials were conducted using finite element modeling to systematically evaluate the influence of each parameter combination. The clearance values ranged from 0.285 to 0.475 mm, punch radius varied from 1.0 to 1.5 mm, and draw ratios were set at 1.69, 2.53, and 3.09. Three lubricants—PTFE, MoS_2, and graphite—were used to assess effects on formability. The resulting simulated responses revealed considerable variability across conditions, with RTF ranging from 7.58 to 21.77 N, SB from 1.24 to 15.9 μm, FLC between 11.5% and 23.2%, and MTR from 1.75 to 14.6, providing a comprehensive dataset for subsequent optimization and fuzzy-based analysis in Table 2.

Fuzzy linguistic descriptor

Table 3 presents the fuzzy linguistic descriptors and their corresponding Intuitionistic Fuzzy Numbers (IFNs), which define the relative importance of criteria in decision-making. Five levels of importance are considered: Very Important (VI), Important (I), Medium (M), Unimportant (UI), and Very Unimportant (VU). Each level is expressed in terms of three values: membership (μ), non-membership (ν), and hesitation (π). For example, the "Very Important" (VI) level is characterized by a high membership degree ($\mu = 0.88$), reflecting strong preference, along with a low non-membership degree ($\nu = 0.08$) and a small hesitation degree ($\pi = 0.04$), indicating minimal uncertainty in the decision-making process. The "Important" (I) category has $\mu = 0.75$, $\nu = 0.20$, and $\pi = 0.05$, showing a significant preference with slight uncertainty. The "Medium" (M) descriptor, with $\mu = 0.50$, $\nu = 0.45$, and $\pi = 0.05$, reflects a balanced state, indicating neutrality with equal preference and non-preference. The "Unimportant" (UI) level, with $\mu = 0.35$, $\nu = 0.60$, and $\pi = 0.05$, indicates a lower preference, suggesting the criterion is less relevant. Lastly, the "Very Unimportant" (VU) category has $\mu = 0.08$, $\nu = 0.88$, and $\pi = 0.04$, reflecting strong non-preference and near-complete insignificance in decision-making. These IFNs provide a structured approach to handle uncertainty in multi-criteria decision analysis, ensuring a more flexible and robust evaluation of importance across different scenarios.

	Input				Simulation result			
Trail runs	Clearance, C	Punch radius, *R*	Draw ratio	Dry lubricants	RTF (*N*)	SB (μm)	FLC (%)	MTR
1	0.35	1.5	1.69	PTFE	13.1490	14.628	18.1888	13.6864
2	0.475	1.5	1.69	MoS2	12.9313	8.84041	16.1008	8.736
3	0.285	1.5	1.69	MoS2	8.9257	11.8932	14.3376	12.02656
4	0.475	1.5	1.69	Graphite	21.77	10.0488	20.1376	6.66848
5	0.285	1.5	1.69	Graphite	17.416	11.8932	20.9728	10.25024
6	0.35	1.25	1.69	Graphite	12.7136	10.0488	17.168	8.7368
7	0.285	1	2.53	Graphite	12.2782	10.0488	17.632	8.7361
8	0.285	1.5	2.53	PTFE	15.239	12.9108	18.563	11.5024
9	0.475	1.25	2.53	PTFE	21.77	4.7701	23.223	1.751
10	0.475	1.25	2.53	PTFE	9.9706	8.8404	15.2192	6.9888
11	0.475	1	2.53	Graphite	7.5759	14.0556	11.5072	11.32768
12	0.475	1	2.53	MoS2	11.6251	10.0488	16.1008	8.7361
13	0.35	1.25	3.09	MoS2	12.8443	15.9087	16.6112	14.56
14	0.285	1	3.09	Graphite	9.92712	11.3208	15.544	9.9008
15	0.35	1.25	3.09	PTFE	21.2039	3.0528	21.0192	2.06752
16	0.35	1.5	3.09	MoS2	11.1897	8.8404	18.56	8.7361
17	0.285	1	3.09	PTFE	17.8949	1.2402	17.632	2.70816
18	0.285	1	3.09	MoS2	8.18552	11.3208	12.8528	9.08544

Table 2. Simulated response.

Fuzzy linguistic descriptor		Very Important - VI	Important - I	Medium - M	Unimportant - UI	Very Unimportant - VU
IF number	μ	0.880	0.750	0.50	0.350	0.080
	ν	0.080	0.20	0.450	0.600	0.880
	π	0.040	0.050	0.050	0.050	0.040

Table 3. Fuzzy linguistic descriptor.

Decision makers	IF number			Weight of DM	
	μ	ν	π		
DM1 - VI	0.880	0.080	0.040	0.920	0.291
DM2 - VI	0.880	0.080	0.040	0.920	0.291
DM3 - I	0.750	0.200	0.050	0.790	0.251
DM4 - M	0.500	0.450	0.050	0.530	0.167
			SUM	3.150	1.00

Table 4. Linguistic variables for a rating of criteria and DMs.

Linguistic variables for a rating of criteria and DMs

Table 4 shows the linguistic variables used to rate the criteria, along with the assessments provided by four decision makers (DMs), expressed as Intuitionistic Fuzzy Numbers (IFNs). Each importance level is represented by fuzzy linguistic descriptors, such as Very Important (VI), Important (I), and Medium (M), defined by their membership (μ), non-membership (ν), and hesitation (π) degrees. Decision Makers 1 and 2 (DM1 and DM2) both assign the "Very Important" (VI) rating to the criteria, with $\mu = 0.88$, $\nu = 0.08$, and $\pi = 0.04$, reflecting a strong level of confidence and minimal uncertainty. As a result, both DM1 and DM2 are allocated high weights of 0.92 each, contributing equally to the decision-making process with a normalized weight of 0.291. DM3, rating the criteria as Important (I), has slightly lower membership ($\mu = 0.75$) and higher non-membership ($\nu = 0.20$, $\pi = 0.05$), resulting in a decision-maker weight of 0.79 and a normalized weight of 0.251. Meanwhile, DM4, assigning a Medium (M) importance level, has $\mu = 0.50$, $\nu = 0.45$, $\pi = 0.05$, reflecting a more neutral stance, with a decision-maker weight of 0.53 and a normalized weight of 0.167. The sum of all decision-maker weights equals 3.15, ensuring consistency in the weighting process, with the normalized sum equating to 1.00, which ensures the proper distribution of influence among decision-makers in the evaluation process. This structured weighting approach ensures a balanced and objective aggregation of expert opinions, refining the decision-making process through IF-MCDM techniques.

Criteria definition and decision-maker assessments

Table 5 presents the evaluation of 20 criteria (C1–C20) by four decision makers (DM1–DM4) in a robust decision-making framework. Each criterion is assessed based on its importance, using Intuitionistic Fuzzy Linguistic terms (Very Important (VI), Important (I), Medium (M), and Unimportant (UI)), and expressed through corresponding Intuitionistic Fuzzy Numbers (IFNs). The criteria are categorized into four groups based on their response variables. RTF (N): Criteria C1 to C5 relate to the response of RTF (N), which measures the force or resistance to deformation under load. SB (μm): Criteria C6 to C10 correspond to SB (μm), representing surface roughness or texture measurements in micrometers. FLC (%): Criteria C11 to C15 are associated with FLC (%), which refers to the percentage of the FLC, indicating the material's formability in a manufacturing process. MTR: Criteria C16 to C20 are related to MTR, which refers to material properties or characteristics such as tensile strength, ductility, or other mechanical traits. These 20 criteria were evaluated using the ratings from four decision makers. The ratings reveal varying perceptions of importance for each criterion. For instance, Criteria C6, C7, C13, and C14 received unanimous Very Important (VI) ratings from all decision makers, indicating their crucial role in the assessment. In contrast, some criteria, such as C1 and C5, exhibited mixed opinions. C1, for example, was rated Medium (M) by DM1, DM3, and DM4, while DM2 rated it as Important (I). Similarly, C5 was rated Medium (M) by DM1, Important (I) by DM2 and DM3, and Very Important (VI) by DM4. Criteria such as C10 and C17 had mixed ratings, with one decision maker rating them as Very Important (VI) and others rating them as Important (I), reflecting a slight divergence in opinion. A noteworthy example is C20, where the decision makers' ratings varied significantly—DM1 and DM2 rated it as Very Important (VI), DM3 as Important (I), and DM4 as Unimportant (UI), showing considerable differences in perceived importance. The table provides a structured approach to evaluating the criteria, with most rated as Important (I) or Very Important (VI), ensuring that the decision-making framework remains balanced and comprehensive. It is essential to clarify the definitions and context of each criterion, as understanding what is being evaluated is critical for assessing the decision-making process accurately.

Criteria	Kind of criteria	Criteria	DM1	DM2	DM3	DM4
C1	-1	C1	M	I	M	M
C2	-1	C2	I	I	I	M
C3	-1	C3	VI	I	VI	I
C4	-1	C4	I	I	I	I
C5	-1	C5	M	I	I	VI
C6	-1	C6	VI	VI	VI	VI
C7	-1	C7	VI	VI	VI	I
C8	-1	C8	I	M	I	I
C9	-1	C9	I	I	I	I
C10	-1	C10	I	VI	I	I
C11	1	C11	I	I	I	I
C12	1	C12	I	M	I	I
C13	1	C13	VI	VI	VI	VI
C14	1	C14	VI	VI	VI	VI
C15	1	C15	M	M	I	M
C16	1	C16	M	I	I	I
C17	1	C17	I	VI	I	VI
C18	1	C18	I	I	I	I
C19	1	C19	VI	I	I	M
C20	1	C20	VI	VI	I	UI

Table 5. Criteria ratings by decision makers.

Intuitionistic fuzzy evaluation matrix

Supplementary Tables 1–6 collectively provide a detailed representation of the Intuitionistic Fuzzy Multi-Criteria Decision-Making (IF-MCDM) framework applied in this study. Supplementary Table 1, the IF Evaluation Matrix, captures the assessments of four decision makers (DM1–DM4) using Intuitionistic Fuzzy Numbers (μ, ν, π), where 1-μ denotes uncertainty, ν denotes hesitation, and π denotes non-membership. Decision-maker weights are 0.291 for DM1–DM3 and 0.167 for DM4. Consistent ratings for C6, C7, C13 and C14 (0.12, 0.08, 0.04) indicate high importance and minimal uncertainty, whereas C20 shows the greatest variation, with DM4 assigning $\nu = 0.6$ and $1-\mu = 0.65$. Other criteria, such as C1, C5, C15 and C16, exhibit mixed uncertainty and hesitation levels, while C3, C10 and C17 reflect notable differences in perceived significance. Supplementary Table 2, the Weighted Criteria Evaluation Matrix, presents δ^+ (positive deviation), δ^- (negative deviation) and CW (criteria weight), from which normalized weights summing to 1.000 are derived to ensure a balanced prioritization of decision factors. Supplementary Table 3 defines the linguistic variables used by MARCOS for rating alternatives, ranging from "Extremely Good (EG)" = (1.00, 0.00, 0) to "Very Very Bad (VVB)" = (0.10, 0.90, 0.00), illustrating how hesitation and non-membership increase as preference declines. Supplementary Table 4 reports the evaluation of twenty alternatives (A1–A20) against twenty criteria (C1–C20) based on the decision makers' linguistic ratings. Alternatives A5 and A15 consistently receive EG and VVG ratings, marking them as top performers, whereas A9, A12 and A17 obtain mostly lower scores. Supplementary Table 5, the Initial Aggregated Matrix, normalizes all criteria values between 0 and 1, showing A5, A16 and A17 achieving multiple 1.000 scores, while A20 exhibits both high and low extremes, indicating diverse performance. Finally, Supplementary Table 6, the Aggregated IF Decision Matrix, lists δ^+, δ^- and CW for each alternative under all criteria, revealing that A5 and A17 register $\delta^+ = 0$ and $\delta^- = 1.414$, signifying the strongest negative impact, whereas A2, A7 and A14 show lower CW values associated with better decision outcomes. Together, these tables provide a comprehensive, human-interpretable summary of the IF-MARCOS evaluation process, integrating uncertainty, hesitation, and weighted importance to yield a robust, multidimensional analysis of alternative performance.

Extended IF decision matrix

Table 6 presents the Extended Intuitionistic Fuzzy (IF) Decision Matrix, detailing alternative (Alt) evaluations across criteria (C1 to C20). The initial row provides reference values: 0.039, 0.047, 0.053, -, 0.053, 0.055, 0.044, and 0.051, followed by a normalized reference row of 1.000 for all criteria. The alternatives (A1 to A20) exhibit varying degrees of membership values. For instance, A1 records values of 0.643, 0.592, 0.494, -, 0.592, 0.494, 0.589, and 0.643, while A5 and AI (Ideal Alternative) consistently achieve 1.000 across all criteria. A4 displays high values, such as 0.791, 0.825, 0.843, -, 0.825, 0.843, 0.756, and 0.720, whereas AAI (Anti-Ideal Alternative) reflects the lowest values, including 0.306, 0.337, 0.279, -, 0.337, 0.279, 0.433, and 0.263. Alternatives like A8 and A17 also show strong performance, with A8 reaching 1.000 in some criteria, while A17 consistently achieves 1.000 except for the last criterion (0.830). Variations in performance across criteria highlight the decision matrix's role in evaluating multi-criteria decision-making processes using the Intuitionistic Fuzzy approach.

	0.039	0.047	0.053	-	0.053	0.055	0.044	0.051
	1.000	1.000	1.000	-	1.000	1.000	1.000	1.000
Alt	C1	C2	C3	-	C17	C18	C19	C20
A1	0.643	0.592	0.494	-	0.592	0.494	0.589	0.643
A2	0.367	0.468	0.433	-	0.468	0.433	0.433	0.263
A3	0.689	0.651	0.575	-	0.651	0.575	0.689	0.643
A4	0.791	0.825	0.843	-	0.825	0.843	0.756	0.720
A5	1.000	1.000	1.000	-	1.000	1.000	1.000	1.000
A6	0.478	0.596	0.592	-	0.596	0.592	0.534	0.741
A7	0.306	0.433	0.279	-	0.433	0.279	0.494	1.000
A8	0.849	0.849	1.000	-	0.849	1.000	0.831	0.575
A9	0.405	0.367	0.451	-	0.367	0.451	0.617	0.843
A10	0.756	0.643	0.604	-	0.643	0.604	0.741	0.830
A11	0.849	0.468	0.468	-	0.595	0.635	0.671	0.653
A12	0.405	0.651	0.651	-	0.604	0.736	0.690	1.000
A13	0.494	0.494	0.589	-	0.494	0.589	0.494	0.623
A14	0.337	0.337	0.433	-	0.337	0.433	0.433	1.000
A15	0.689	0.689	0.689	-	0.689	0.689	0.575	0.271
A16	1.000	1.000	0.756	-	1.000	0.756	0.843	0.372
A17	1.000	1.000	1.000	-	1.000	1.000	1.000	0.830
A18	0.720	0.720	0.534	-	0.720	0.534	0.592	0.653
A19	0.494	0.494	0.720	-	0.849	0.720	0.720	0.720
A20	0.337	0.337	1.000	-	0.405	1.000	1.000	1.000
AI	1.000	1.000	1.000	-	1.000	1.000	1.000	1.000
AAI	0.306	0.337	0.279	-	0.337	0.279	0.433	0.263

Table 6. Extended IF decision matrix.

Normalized IF decision matrix

Table 7 presents the Normalized Intuitionistic Fuzzy (IF) Decision Matrix, displaying alternative (Alt) evaluations across criteria (C1 to C20, with C17 omitted). The initial row contains reference values: 0.039, 0.047, 0.053, -, 0.055, 0.044, and 0.051, followed by a normalized reference row with all values set to 1.000. The alternatives (A1 to A20) demonstrate varying degrees of membership values. A1 records values of 0.643, 0.592, 0.494, -, 0.494, 0.589, and 0.643, while A5 and AI (Ideal Alternative) achieve consistent values of 1.000 across all criteria. A4 exhibits strong performance with values like 0.791, 0.825, 0.843, -, 0.843, 0.756, and 0.720, whereas AAI (Anti-Ideal Alternative) shows the lowest values, such as 0.306, 0.337, 0.279, -, 0.279, 0.433, and 0.263. Alternatives like A8 and A17 also perform well, with A8 achieving 1.000 in select criteria, and A17 maintaining 1.000 except for the last criterion (0.830). The matrix facilitates multi-criteria decision-making by normalizing the IF values, ensuring comparability across alternatives.

Weighted IF decision matrix

Table 8 presents the Weighted Intuitionistic Fuzzy (IF) Decision Matrix, where alternative (Alt) evaluations are adjusted by their respective criterion weights across C1 to C20 (excluding C17). The highest values are consistently observed for A5 and AI (Ideal Alternative), both achieving 0.039, 0.047, 0.053, 0.055, 0.044, and 0.051, reflecting optimal performance across all criteria. A4 exhibits strong weighted values, particularly in C18 (0.047) and C3 (0.045), while A8 and A17 also maintain high scores, with A8 achieving 0.053 in C3 and A17 mirroring AI in all but the last criterion (0.043). Conversely, AAI (Anti-Ideal Alternative) records the lowest values, such as 0.012, 0.016, 0.015, -, 0.015, 0.019, and 0.013, representing the least favorable performance. Intermediate alternatives like A10 and A15 show moderate weighting distributions, with A10 reaching 0.032 in C3 and A15 balancing values across criteria. This matrix facilitates multi-criteria decision-making by incorporating weight-based adjustments, ensuring a refined comparative analysis of alternatives.

Utility degrees and utility functions

Table 9 presents the Utility Functions of Alternatives, evaluating performance through parameters Si, Ki-, Ki+, f(K-), f(K+), and derived utility functions. The highest-ranked alternative, A5, achieves a utility function value of 0.892 with Si = 0.952, Ki- = 3.214, and Ki + = 0.952, indicating optimal performance. Following closely, A17 (0.826) and A20 (0.785) rank second and third, respectively, demonstrating strong utility values. A12 (0.715) and A4 (0.700) perform well, ranking fourth and fifth, respectively. Mid-ranked alternatives such as A10 (0.671), A19 (0.678), and A16 (0.682) exhibit moderate utility values. The lowest-ranked alternative, A2, records a utility function value of 0.388, with Si = 0.414, indicating the least favorable performance. The Ideal Alternative (AI) achieves the highest possible score, while the Anti-Ideal Alternative (AAI) has the lowest Si value (0.296),

	0.039	0.047	0.053	-	0.055	0.044	0.051
	1.000	1.000	1.000	-	1.000	1.000	1.000
Alt	C1	C2	C3	-	C18	C19	C20
A1	0.643	0.592	0.494	-	0.494	0.589	0.643
A2	0.367	0.468	0.433	-	0.433	0.433	0.263
A3	0.689	0.651	0.575	-	0.575	0.689	0.643
A4	0.791	0.825	0.843	-	0.843	0.756	0.720
A5	1.000	1.000	1.000	-	1.000	1.000	1.000
A6	0.478	0.596	0.592	-	0.592	0.534	0.741
A7	0.306	0.433	0.279	-	0.279	0.494	1.000
A8	0.849	0.849	1.000	-	1.000	0.831	0.575
A9	0.405	0.367	0.451	-	0.451	0.617	0.843
A10	0.756	0.643	0.604	-	0.604	0.741	0.830
A11	0.849	0.468	0.468	-	0.635	0.671	0.653
A12	0.405	0.651	0.651	-	0.736	0.690	1.000
A13	0.494	0.494	0.589	-	0.589	0.494	0.623
A14	0.337	0.337	0.433	-	0.433	0.433	1.000
A15	0.689	0.689	0.689	-	0.689	0.575	0.271
A16	1.000	1.000	0.756	-	0.756	0.843	0.372
A17	1.000	1.000	1.000	-	1.000	1.000	0.830
A18	0.720	0.720	0.534	-	0.534	0.592	0.653
A19	0.494	0.494	0.720	-	0.720	0.720	0.720
A20	0.337	0.337	1.000	-	1.000	1.000	1.000
AI	1.000	1.000	1.000	-	1.000	1.000	1.000
AAI	0.306	0.337	0.279	-	0.279	0.433	0.263

Table 7. Normalized matrix.

Alt	C1	C2	C3	-	C18	C19	C20
A1	0.025	0.028	0.026	-	0.027	0.026	0.033
A2	0.014	0.022	0.023	-	0.024	0.019	0.013
A3	0.027	0.030	0.031	-	0.032	0.030	0.033
A4	0.031	0.038	0.045	-	0.047	0.033	0.037
A5	0.039	0.047	0.053	-	0.055	0.044	0.051
A6	0.018	0.028	0.032	-	0.033	0.023	0.038
A7	0.012	0.020	0.015	-	0.015	0.021	0.051
A8	0.033	0.039	0.053	-	0.055	0.036	0.029
A9	0.016	0.017	0.024	-	0.025	0.027	0.043
A10	0.029	0.030	0.032	-	0.033	0.032	0.043
A11	0.033	0.022	0.025	-	0.035	0.029	0.033
A12	0.016	0.030	0.035	-	0.041	0.030	0.051
A13	0.019	0.023	0.031	-	0.033	0.022	0.032
A14	0.013	0.016	0.023	-	0.024	0.019	0.051
A15	0.027	0.032	0.037	-	0.038	0.025	0.014
A16	0.039	0.047	0.040	-	0.042	0.037	0.019
A17	0.039	0.047	0.053	-	0.055	0.044	0.043
A18	0.028	0.033	0.028	-	0.029	0.026	0.033
A19	0.019	0.023	0.038	-	0.040	0.031	0.037
A20	0.013	0.016	0.053	-	0.055	0.044	0.051
AI	0.039	0.047	0.053	-	0.055	0.044	0.051
AAI	0.012	0.016	0.015	-	0.015	0.019	0.013

Table 8. Weighted intuitionistic fuzzy decision matrix.

Alt	Si	Ki-	Ki+	f(K-)	f(K+)	(1-f(K-))/f(K-)	(1-f(K+))/f(K+)	f(K)	Ranking
A1	0.592	1.997	0.592	0.229	0.771	3.375	0.296	0.554	17
A2	0.414	1.397	0.414	0.229	0.771	3.375	0.296	0.388	20
A3	0.640	2.161	0.640	0.229	0.771	3.375	0.296	0.600	13
A4	0.747	2.522	0.747	0.229	0.771	3.375	0.296	0.700	5
A5	0.952	3.214	0.952	0.229	0.771	3.375	0.296	0.892	1
A6	0.627	2.117	0.627	0.229	0.771	3.375	0.296	0.587	15
A7	0.643	2.172	0.643	0.229	0.771	3.375	0.296	0.603	12
A8	0.664	2.242	0.664	0.229	0.771	3.375	0.296	0.622	11
A9	0.532	1.797	0.532	0.229	0.771	3.375	0.296	0.499	19
A10	0.716	2.418	0.716	0.229	0.771	3.375	0.296	0.671	8
A11	0.670	2.262	0.670	0.229	0.771	3.375	0.296	0.628	9
A12	0.763	2.576	0.763	0.229	0.771	3.375	0.296	0.715	4
A13	0.601	2.029	0.601	0.229	0.771	3.375	0.296	0.563	16
A14	0.638	2.153	0.638	0.229	0.771	3.375	0.296	0.597	14
A15	0.589	1.989	0.589	0.229	0.771	3.375	0.296	0.552	18
A16	0.728	2.458	0.728	0.229	0.771	3.375	0.296	0.682	6
A17	0.882	2.977	0.882	0.229	0.771	3.375	0.296	0.826	2
A18	0.668	2.256	0.668	0.229	0.771	3.375	0.296	0.626	10
A19	0.724	2.443	0.724	0.229	0.771	3.375	0.296	0.678	7
A20	0.838	2.828	0.838	0.229	0.771	3.375	0.296	0.785	3
AI	1								
AAI	0.296								

Table 9. Utility evaluation and ranking alternatives.

signifying the worst-case scenario. This utility-based ranking facilitates decision-making by quantitatively distinguishing between the alternatives based on their computed utility functions.

Effects on contour plots of RTF – clearance vs. punch radius vs. draw ratio

Figure 6: Radial Tool Force (RTF) results are summarized for different conditions and lubricants. Figure 6a shows that larger punch radii and higher clearances reduce RTF for PTFE lubrication. Figure 6b, higher draw ratios increase tensile forces, while higher clearances reduce tool contact. Figure 6c demonstrates that increased punch radius raises RTF due to more deformation, with PTFE reducing the impact of the draw ratio. Figure 6d, small clearances and large punch radii cause sharp RTF increases with MoS2 lubrication. Figure 6e shows that higher draw ratios and smaller clearances increase RTF under MoS2. Figure 6f indicates significant non-linearity with MoS2, as large punch radii lead to localized stretching and higher RTF. For Graphite, Fig. 6g highlights steep RTF increases due to high friction with larger punch radii. Figure 6h, high draw ratios and low clearances under Graphite lubrication result in heightened tensile forces. Finally, Fig. 6i shows that maximum RTF occurs with large punch radii and high draw ratios due to Graphite's high friction.

Effects on contour plots of spring back – clearance vs. punch radius vs. draw ratio

Figure 7: Springback (SB) behaviour is analyzed for different conditions and lubricants. In Fig. 7a, larger punch radii increase springback for PTFE lubrication, with higher clearance slightly mitigating recovery. Figure 7b shows that higher clearances and moderate draw ratios reduce springback due to more uniform plastic deformation. Figure 7c, springback increases linearly with punch radius due to enhanced elastic recovery. Figure 7d indicates that small clearances under MoS2 lubrication amplify elastic recovery due to increased contact. Figure 7e, higher draw ratios under MoS2 increase springback due to deeper plastic deformation. Figure 7f highlights that larger punch radii under MoS2 cause higher springback due to increased bending stresses. For Graphite lubrication, Fig. 7g shows steep springback increases due to high friction. Figure 7h, small clearances and high draw ratios intensify elastic recovery under Graphite. Finally, in Fig. 7i, maximum springback is observed at high punch radii and draw ratios due to Graphite's frictional stress buildup.

Effects on contour plots of FLC (%)– clearance vs. punch radius vs. draw ratio

Figure 8: FLC %, behaviour is evaluated under different conditions and lubricants. In Fig. 8a, optimal formability is achieved with moderate clearance and small punch radius under PTFE lubrication, balancing strain without fracture. Figure 8b shows that moderate clearance and draw ratio improve formability by preventing strain localization. Figure 8c, a small punch radius promotes uniform strain distribution under PTFE. Figure 8d indicates that increased punch radius reduces formability under MoS2 due to localized stretching. Figure 8e, balanced clearance and draw ratio improve formability with MoS2. Figure 8f shows that excessive punch radius reduces FLC under MoS2 by amplifying strain. For Graphite lubrication, Fig. 8g highlights that high friction increases localized thinning, lowering formability. Figure 8h, higher draw ratios under Graphite cause strain

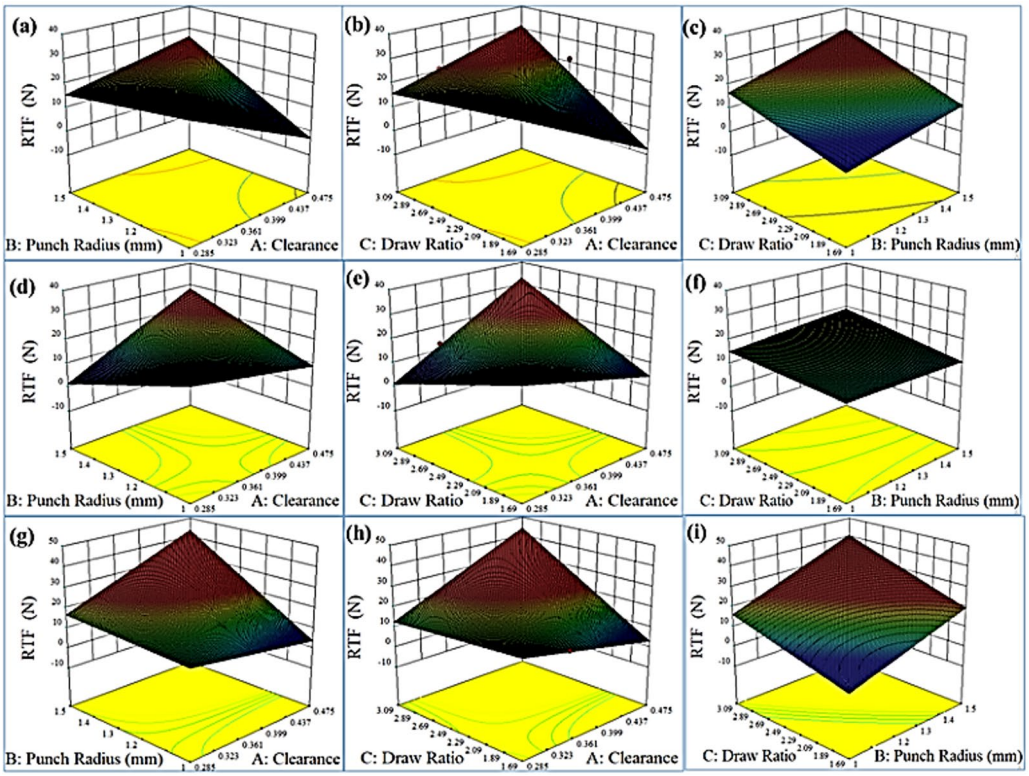

Fig. 6. RTF, PTFE (**a**) Clearance vs. punch radius, (**b**) Clearance vs. draw ratio, (**c**) Punch radius vs. draw ratio, MoS2, (**d**) Clearance vs. punch radius, (**e**) Clearance vs. draw ratio, (**f**) Punch radius vs. draw ratio, graphite (**g**) Clearance vs. punch radius, (**h**) Clearance vs. draw ratio, (**i**) Punch radius vs. draw ratio.

localization, further reducing FLC. Finally, in Fig. 8i, large punch radii and high friction under Graphite reduce formability due to excessive thinning.

Effects on contour plots of MTR– clearance vs. punch radius vs. draw ratio
Figure 9: Material Thinning Rate (MTR) is influenced by various factors under different lubrication conditions. In subplot (a), higher punch radius causes material thinning under PTFE due to increased stretching. Figure 9b shows that higher clearance under PTFE reduces thinning by limiting friction and deformation. Figure 9c, thinning increases with larger punch radius due to localized deformation. For MoS2 lubrication, Fig. 9d indicates increased thinning with smaller clearance and larger punch radius due to enhanced stretching. Figure 9e shows that moderate clearance reduces stress concentration and limits thinning. Figure 9f, thinning rises rapidly at high punch radius under MoS2 due to localized plastic deformation. For Graphite lubrication, Fig. 9g highlights that larger punch radius causes significant thinning due to high friction. Figure 9h shows excessive thinning with high draw ratio and small clearance under Graphite. Finally, Fig. 9i, a high punch radius under Graphite lubrication amplifies thinning due to friction and deformation forces.

Predicted vs. actual

Figure 10 presents the Predicted vs. Actual plots for Fig. 10a Clearance, Fig. 10b Punch Radius, Fig. 10c Draw Ratio, and Fig. 10d Dry Lubricants, highlighting the model's predictive accuracy. The close alignment of data points along the diagonal reference line across all subplots indicates a strong correlation between predicted and actual values, suggesting high model reliability. Figure 10a shows minimal deviation, confirming precise predictions for Clearance. In Fig. 10b, Punch Radius exhibits slight scattering, implying minor inconsistencies in prediction accuracy. The Draw Ratio in Fig. 10c follows the trend closely, though a few outliers suggest local variations. Similarly, Fig. 10d Dry Lubricants demonstrates strong alignment with a few deviations. These results validate the model's capability to capture underlying relationships, with minor improvements needed in specific cases for enhanced precision.

Validation through residual plots

Figure 11 displays Predicted vs. Externally Studentized Residuals for Fig. 11a Clearance, Fig. 11b Punch Radius, Fig. 11c Draw Ratio, and Fig. 11d Dry Lubricants, assessing error distribution and model validity. The random dispersion of residuals around zero across all subplots suggests that the model does not exhibit bias and maintains homoscedasticity. In Fig. 11a, Clearance shows a well-distributed residual pattern, indicating stable predictions. However, Fig. 11b Punch Radius and Fig. 11c Draw Ratio exhibit slight clustering of residuals, suggesting localized inconsistencies that may require further refinement. Subplot Fig. 11d for Dry Lubricants

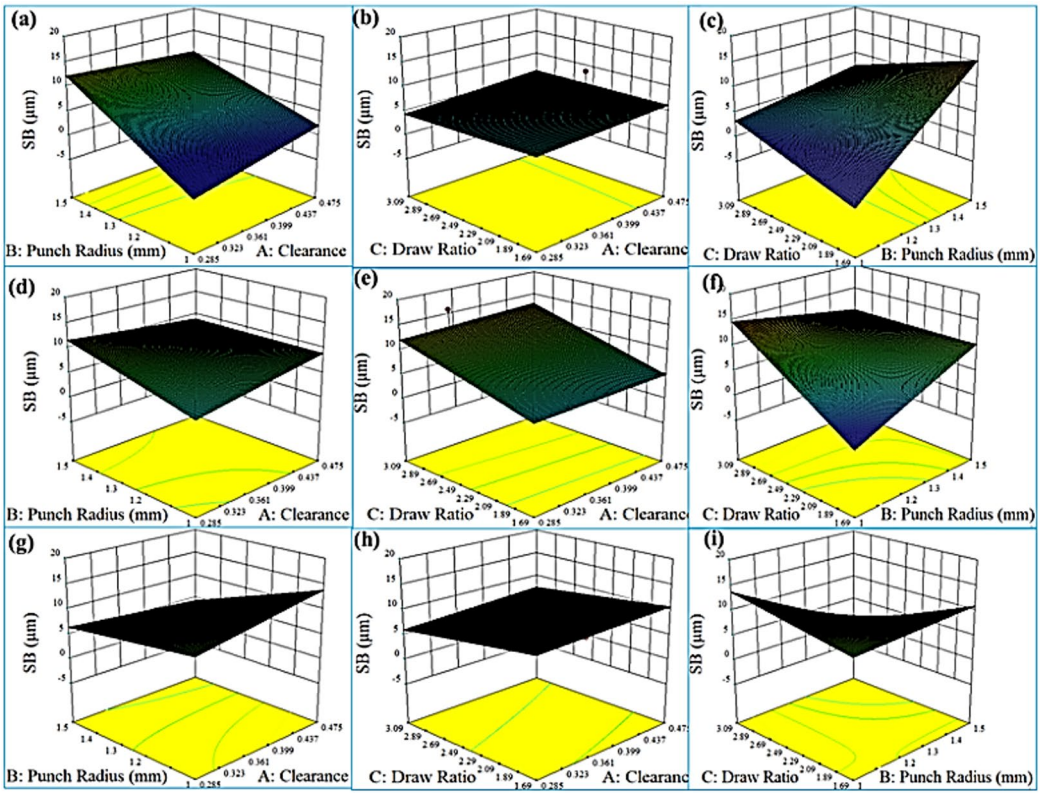

Fig. 7. Spring back, PTFE (**a**) Clearance vs. punch radius, (**b**) Clearance vs. draw ratio, (**c**) Punch radius vs. draw ratio, MoS2, (**d**) Clearance vs. punch radius, (**e**) Clearance vs. draw ratio, (**f**) Punch radius vs. draw ratio, graphite (**g**) Clearance vs. punch radius, (**h**) Draw ratio, (**i**) Punch radius vs. draw ratio.

shows relatively stable residual distribution, with most data points falling within acceptable limits. The overall analysis confirms that the model maintains a balanced residual distribution, ensuring robustness with minor areas for improvement.

Residuals analysis across experimental runs

Figure 12 presents Run Number vs. Externally Studentized Residuals for Fig. 12a Clearance, Fig. 12b Punch Radius, Fig. 12c Draw Ratio, and Fig. 12d Dry Lubricants, evaluating the model's consistency over different experimental runs. The residuals in Fig. 12a Clearance remain evenly distributed with no systematic patterns, indicating stability. In Fig. 12b, Punch Radius shows minor fluctuations, suggesting that prediction errors are not entirely random and may require fine-tuning. Figure 12c Draw Ratio exhibits noticeable deviations in certain runs, pointing to localized variability that should be addressed. Meanwhile, Fig. 12d Dry Lubricants maintains a relatively stable trend with slight oscillations. The overall analysis suggests that the model is robust across multiple runs, with only minor deviations in specific parameters requiring further optimization for enhanced predictive accuracy.

Product quality validation

Microstructural analysis

Figure 13: Microstructural Analysis of the Fabricated Cup, Fig. 13a,e — EBSD Images (Worse vs. Best Conditions): The visual comparison shows noticeable differences in the surface integrity and deformation uniformity. The cup formed under best conditions Fig. 13e exhibits a smooth and intact geometry, whereas the worse condition (a) displays signs of wrinkling and local thinning near the rim and nose. Figure 13b,f — Cup Base (EBSD): The worse condition Fig. 13b reveals a heterogeneous grain structure with elongated grains and signs of deformation bands, suggesting high local strain. In contrast, the best condition Fig. 13f shows equiaxed and refined grains, indicating dynamic recrystallization and uniform deformation at the base. Figure 13c,g — Cup Nose Radius (EBSD): Under worse conditions, Fig. 13c, the nose region displays highly distorted grains with clear evidence of shear localization. The best condition Fig. 13g presents a finer and more homogenous grain orientation, suggesting reduced strain concentration and smoother material flow at the nose. (d) & (h) — Cup Wall (EBSD): The wall region under worse conditions Fig. 13d is characterized by elongated grains and texture gradients, showing uneven deformation. The best condition Fig. 13h offers more refined and uniform grains, indicating improved strain distribution along the wall height. Optimized forming parameters improve grain refinement and microstructural uniformity across all cup regions, minimizing strain localization and enhancing formability.

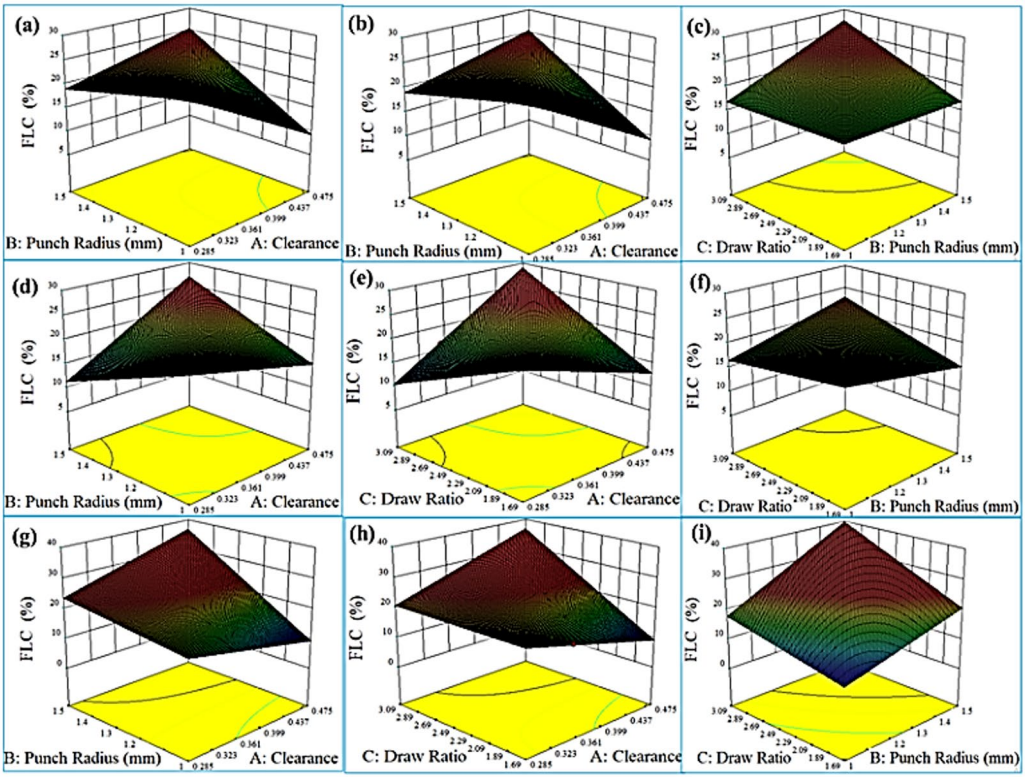

Fig. 8. FLC (%), PTFE (**a**) Clearance vs. punch radius, (**b**) Clearance vs. draw ratio, (**c**) Punch radius vs. draw ratio, MoS2, (**d**) Clearance vs. punch radius, (**e**) Clearance vs. draw ratio, (**f**) Punch radius vs. draw ratio, graphite (**g**) Clearance vs. punch radius, (**h**) Clearance vs. draw ratio, (**i**) Punch radius vs. draw ratio.

Surface roughness

The experiment evaluated the effects of lubricant type and tool-sheet clearance in Incremental Sheet Metal Forming (ISMF) on surface roughness, dimensional accuracy, wall thickness, and springback in Table 10. The best performance was observed in Trial 5 (Graphite, 0.285 mm clearance) with a low surface roughness (0.28 µm), high dimensional accuracy (98.5%), uniform wall thickness (0.32 mm), and minimal springback (2.1). Graphite, acting as a solid lubricant, reduced friction and ensured smooth tool movement, leading to controlled material flow and minimal defects. In contrast, Trial 2 (MoS_2, 0.475 mm clearance) resulted in poor surface quality (0.47 µm roughness), lower accuracy (92.3%), thinner walls (0.26 mm), and higher springback (4.8) due to inconsistent lubrication, excessive material thinning, and increased tool chatter. The cup walls and base in Trial 5 were uniform and accurate, whereas Trial 2 showed rough, uneven deformation with reduced profile stability. The results confirm that graphite lubricant and a tighter clearance enhance formability, reduce defects, and improve final part quality, making it the preferred choice for achieving optimal ISMF performance (Fig. 14).

Figure 15: Surface Topography of Fabricated Cup, Fig. 15a,e — Cup Base Topography (3D Profilometry): The worse condition (a) shows pronounced surface roughness and waviness at the base, possibly due to uneven material stretching. The best condition (e) demonstrates a smoother base with minimal surface defects, indicating better material control. Figure 15b,f — Cup Nose Radius Topography: Significant surface asperities and micro-cracks are visible under worse conditions (b), pointing to tool-material interface issues. In contrast, the best condition (f) exhibits a uniform and defect-free topography, showing successful stress accommodation at the nose. Figure 15c,g — Cup Wall Topography: The worse condition (c) reveals inconsistent wall thickness and roughness bands, suggesting process instability. Under the best condition (g), the wall displays smoother texture and better dimensional fidelity, indicating uniform flow. Figure 15d,h — Full Cup Profile: The worse profile (d) shows overall waviness, indicating surface instability, while the best condition (h) maintains a regular and low-roughness surface, reinforcing process consistency. Best conditions ensure smoother surface topography at the base, nose, and wall, which is crucial for micro-part functionality and performance reliability.

Dimensional accuracy

Dimensional accuracy of the fabricated micro-cups was evaluated using Coordinate Measuring Machine (CMM) and Optical Profilometry to compare the actual dimensions with the design specifications. As presented in Table 11, the micro-cup formed under the best-case conditions demonstrated excellent conformity to the intended geometry, with a base diameter of 1.859 mm, wall height of 4.601 mm, corner radius of 0.199 mm, and wall thickness of 0.188 mm, resulting in a total dimensional deviation of just 0.004 mm, thereby confirming its high accuracy. In contrast, the worst-case sample showed significant deviation from design targets, with a base

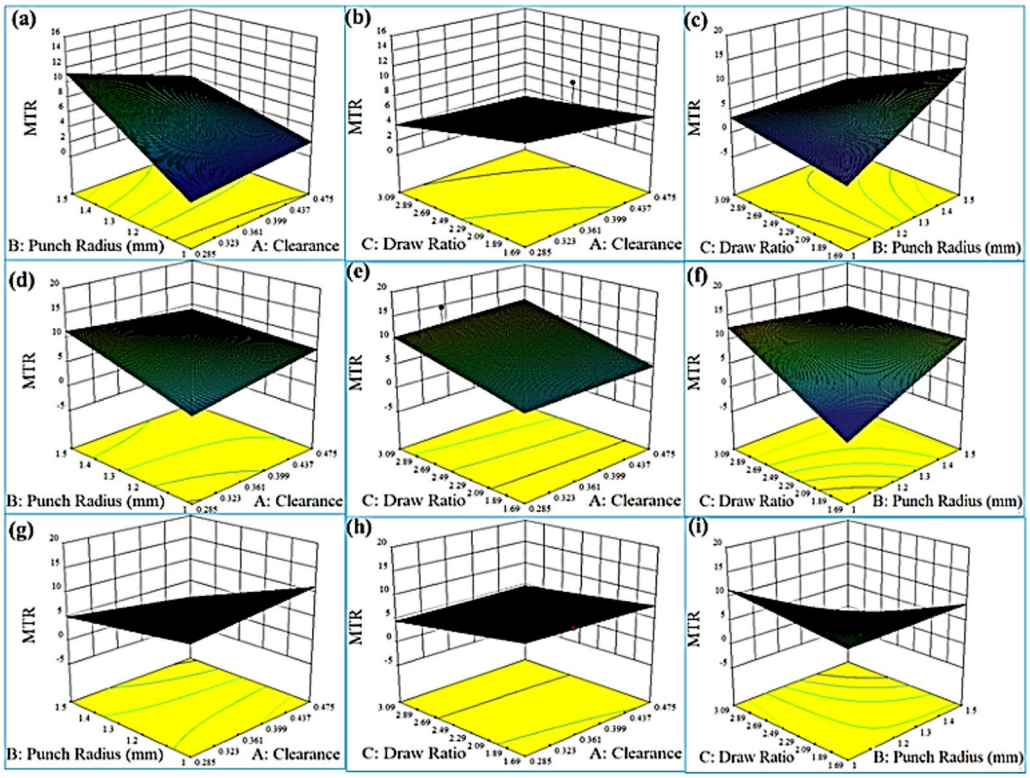

Fig. 9. MTR, PTFE (**a**) Clearance vs. punch radius, (**b**) Clearance vs. draw ratio, (**c**) Punch radius vs. draw ratio, MoS2, (**d**) Clearance vs. punch radius, (**e**) Clearance vs. draw ratio, (**f**) Punch radius vs. draw ratio, graphite (**g**) Clearance vs. punch radius, (**h**) Clearance vs. draw ratio, (**i**) Punch radius vs. draw ratio.

diameter of 1.823 mm, wall height of 4.471 mm, corner radius of 0.231 mm, and wall thickness of 0.173 mm, culminating in a total deviation of 0.134 mm and thus classified as having poor accuracy. These findings reinforce the critical importance of optimized forming parameters to ensure dimensional precision in micro-forming applications and highlight the effectiveness of CMM and optical profilometry in validating geometric consistency.

Figure 16 presents the Dimensional Accuracy of Fabricated Cup, In the best forming condition (Fig. 16a), the thickness increases steadily along the curvilinear distance from base to wall, with relatively minor deviations. This consistency indicates uniform material flow, stable strain distribution, and minimal thinning or thickening across the cup structure. It also reflects well-controlled tooling parameters, which maintained wall integrity and reduced local strain concentrations. Conversely, under the worse condition (Fig. 16b), abrupt variations in thickness are evident, particularly between 6 and 12 mm along the curvilinear path. These oscillations suggest instability in metal flow, possibly caused by excessive friction, poor lubrication, or unoptimized punch/die geometry. Such irregularities can lead to non-uniform wall profiles, reduced part precision, and a higher likelihood of forming defects such as wrinkling or localized necking. The best condition ensures superior dimensional control, critical for high-precision micro-formed parts. Stable thickness progression indicates efficient material deformation and reliable process parameters. In contrast, the worse condition compromises accuracy, increasing the risk of defects and dimensional rejection.

Springback measurement

Figure 17 presents the springback measurements of the fabricated micro-cups made from rolled copper measurement done by profile scanning to validate the accuracy and forming predictions, comparing the best and worst forming conditions to assess geometric accuracy and elastic recovery post-forming. The micro-cup shown in Fig. 17e–h, formed under less favorable conditions, exhibits significantly higher deviation metrics, with the springback angle reaching 1.45° at position Fig. 17f and dimensional deviations of 0.245 mm at Fig. 17g and 0.19 mm at Fig. 17h. These large values suggest a high degree of elastic recovery and reduced form accuracy, indicating insufficient control over material flow and forming pressure. Conversely, the micro-cup in Fig. 17a–d, fabricated under optimal conditions, demonstrates superior dimensional precision with a minimal springback angle of 0.12° at Fig. 17b and very low deviations—0.018 mm at Fig. 17c and 0.01 mm at Fig. 17d—indicating excellent form retention and minimal elastic recovery. These results confirm that optimal forming conditions substantially minimize springback, ensuring better dimensional accuracy and structural integrity of the formed micro-components. Thus, the micro-cup in Fig. 17a–d clearly represents the best mechanical outcome, while the one in Fig. 17e–h highlights the detrimental effects of suboptimal processing on geometrical fidelity.

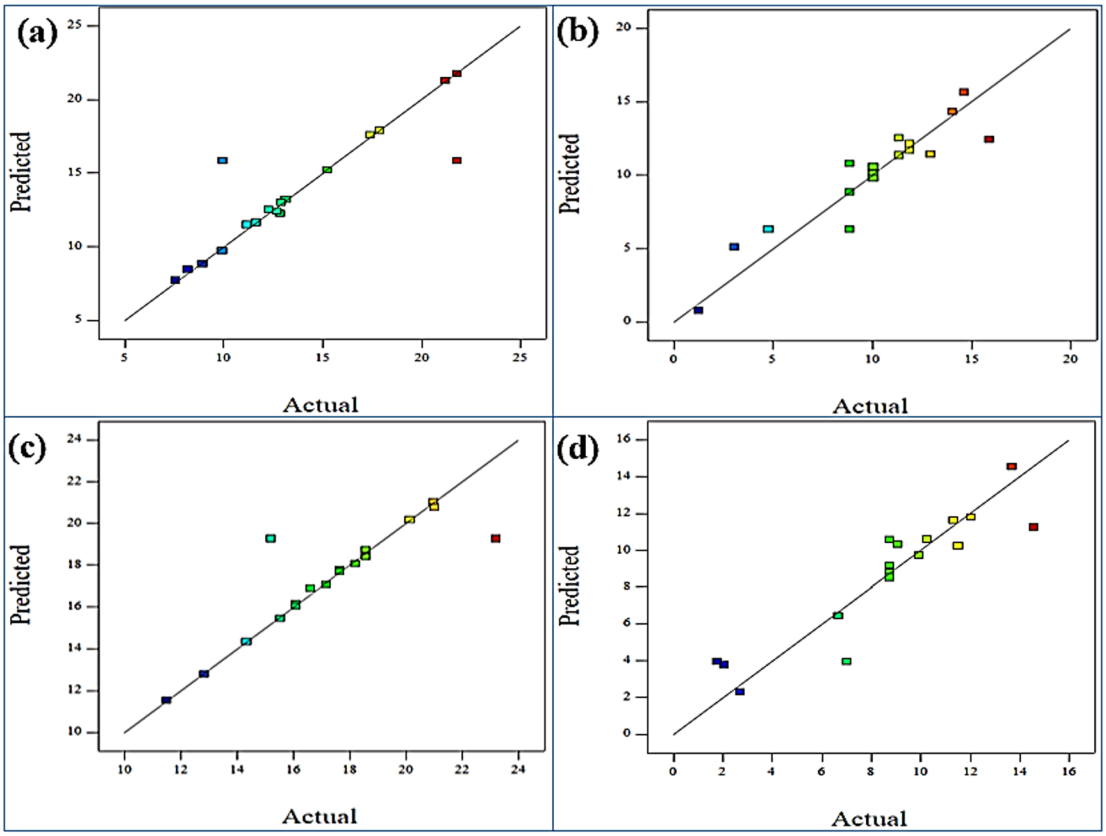

Fig. 10. Predicted vs. Actual, (**a**) Clearance, (**b**) Punch radius, (**c**) Draw ratio, (**d**) Dry lubricants.

Forming limit curve (FLC) validation

Figure 18 is the FLC of Fabricated Cup, The FLC under the best condition (Fig. 18a) shows a broader safe strain zone, with a well-defined curve that remains above the failure threshold across both negative and positive minor strains. The major strain values are higher without approaching the necking limit, indicating enhanced formability. This suggests that under optimal settings, the material undergoes more uniform plastic deformation, with better strain accommodation across the cup base, nose, and wall. In contrast, the worse condition (Fig. 18b) exhibits a steep decline in the FLC, particularly in the negative minor strain region (cup wall thinning), reaching the failure zone earlier. This implies susceptibility to localized thinning or premature fracture due to high strain gradients, poor stress distribution, or non-homogeneous deformation—especially at the cup wall and nose radius. Best forming conditions elevate the material's forming limits, expanding the safe deformation envelope and reducing the risk of early failure. This directly supports improved micro-forming reliability. The worse condition limits formability and increases vulnerability to defects, making it unsuitable for consistent micro-component fabrication.

Hardness test

Figure 19 illustrates the Vickers hardness values measured at various locations on two micro-cups fabricated from rolled copper to assess the influence of forming conditions on mechanical properties. In the first micro-cup (Fig. 19a–d, the hardness varied from 80 HV at position Fig. 19c to a maximum of 125 HV at position (d), indicating significant strain hardening and effective plastic deformation in that region. The relatively high hardness at positions Fig. 19b,d (102 HV and 125 HV, respectively) suggests favorable forming conditions that promoted material flow and work hardening. In contrast, the second micro-cup (Fig. 19e–h, fabricated under less optimal conditions, exhibited lower hardness values, with the minimum of 78 HV observed at position Fig. 19g, pointing to inadequate deformation or reduced strain hardening. The highest hardness in this set was 112 HV at position Fig. 19h, still lower than the maximum observed in the first micro-cup. These variations confirm that the micro-cup in Fig. 19a–d was formed under better mechanical conditions, yielding improved strength through strain hardening, while the micro-cup in Fig. 19e–h reflects less effective processing. The results underscore the importance of controlled forming parameters in optimizing the mechanical performance of micro-formed copper components.

DSC

Figure 20 illustrates DSC of Fabricated Cup, under worse conditions (Fig. 20a), the enthalpy values (ΔH) for the cup wall height, base, and nose radius are 0.4239 J/g, 0.1567 J/g, and 0.6707 J/g, respectively. These values indicate higher residual internal stresses and structural non-uniformity in thermo mechanical properties. The

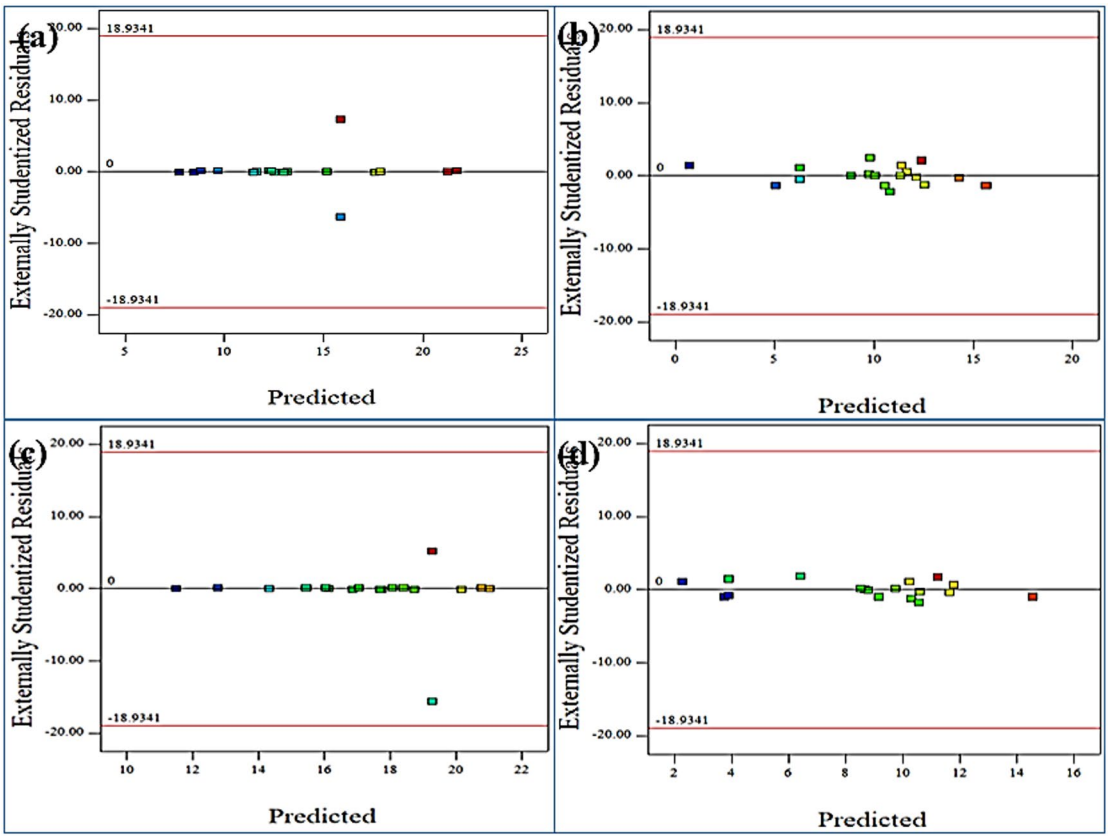

Fig. 11. Predicted vs. externally studentized residuals, predicted vs. actual, (**a**) Clearance, (**b**) Punch radius, (**c**) Draw ratio, (**d**) Dry lubricants.

elevated ΔH for the nose radius suggests significant stored strain energy due to high deformation or rapid cooling, reflecting poor thermal control during forming. Conversely, under best conditions (Fig. 20b), the enthalpy values reduce to 0.0923 J/g (wall), 0.2213 J/g (base), and 0.3223 J/g (nose). These reduced values imply better thermal stability and homogeneity across regions, indicating more uniform plastic deformation and minimal thermal defects. The best condition demonstrates improved thermal behavior, with reduced residual energy and more consistent material transformation. Lower DSC peaks suggest controlled strain distribution and less microstructural disturbance. The worse condition leads to higher residual energy, correlating with poor material flow and higher defect risk.

Sensitivity analysis by mesh sizes

Figure 21 presents the results of a sensitivity analysis conducted with different mesh sizes. The analysis was performed using three distinct scenarios: Scenario 1 with a mesh size of 2.5 µm, Scenario 2 with a mesh size of 7.5 µm, and Scenario 3 with a mesh size of 10 µm. The rankings of the 20 alternatives (A1 to A20) across these three scenarios reveal how the mesh size influences the results, particularly in terms of ranking stability. The variations observed in the rankings between the scenarios provide insights into the effect of mesh refinement on the optimization of the micro-forming process, demonstrating the trade-off between accuracy and computational cost in finite element simulations. The sensitivity analysis suggests that finer meshes (such as Scenario 1) lead to more consistent results, but may incur higher computational demands compared to coarser meshes (such as Scenario 3), where the results may be less sensitive to mesh refinement.

Model validation tests

Force-displacement curve validation

Figure 22: Force–Displacement of Fabricated Cup, The punch load under worse condition (Fig. 22a reaches a peak around ~ 290 N, followed by unstable drops and multiple force fluctuations during displacement. This indicates unstable deformation, possible wrinkling or localized failures, and higher resistance due to friction or tool misalignment. In contrast, the best condition (Fig. 22b) peaks at a lower force (~ 180 N) with a smoother load drop-off, reflecting stable plastic flow, optimized lubrication, and well-coordinated die-punch interaction. The smoother profile suggests less tool-material interaction issues and minimal resistance during wall thinning. The best condition minimizes punch load and ensures smoother material flow, essential for consistent microforming. Reduced peak force also implies less tool wear and energy consumption. The worse condition reflects excessive resistance and material instability, increasing risk of defects and energy inefficiency.

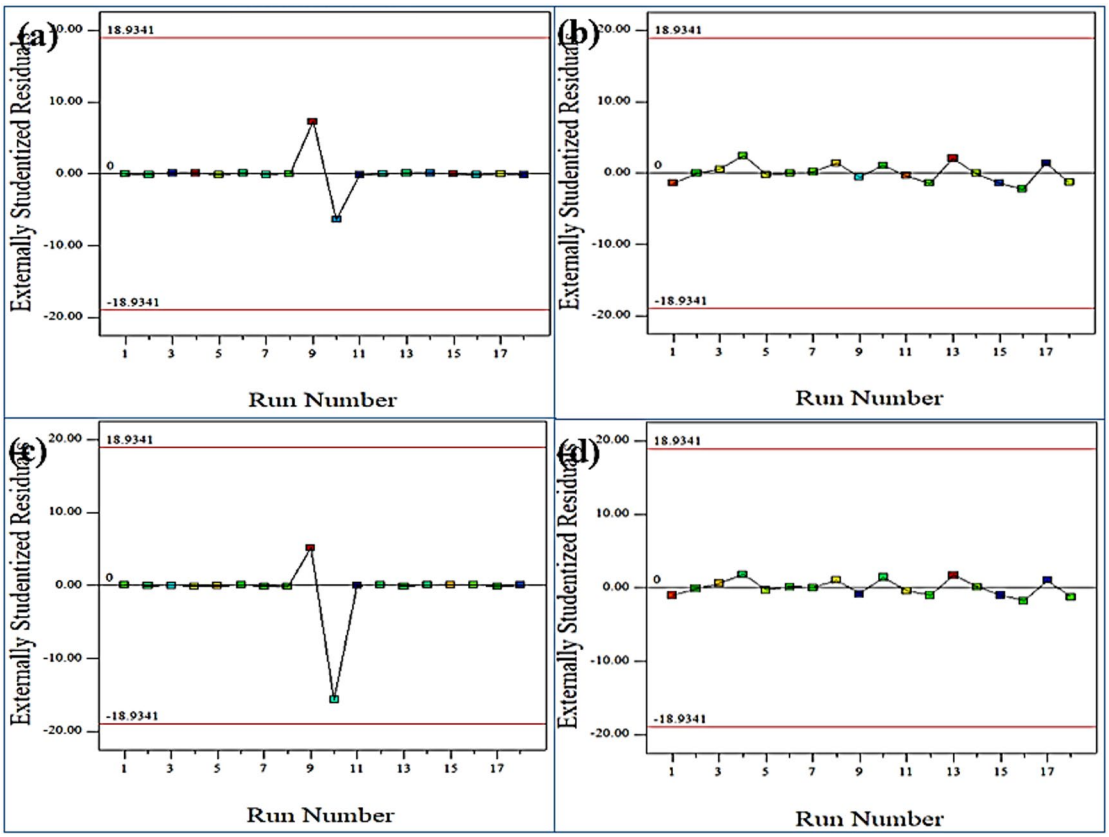

Fig. 12. Run number vs. externally studentized residuals, predicted vs. actual, (**a**) Clearance, (**b**) Punch radius, (**c**) Draw ratio, (**d**) Dry lubricants.

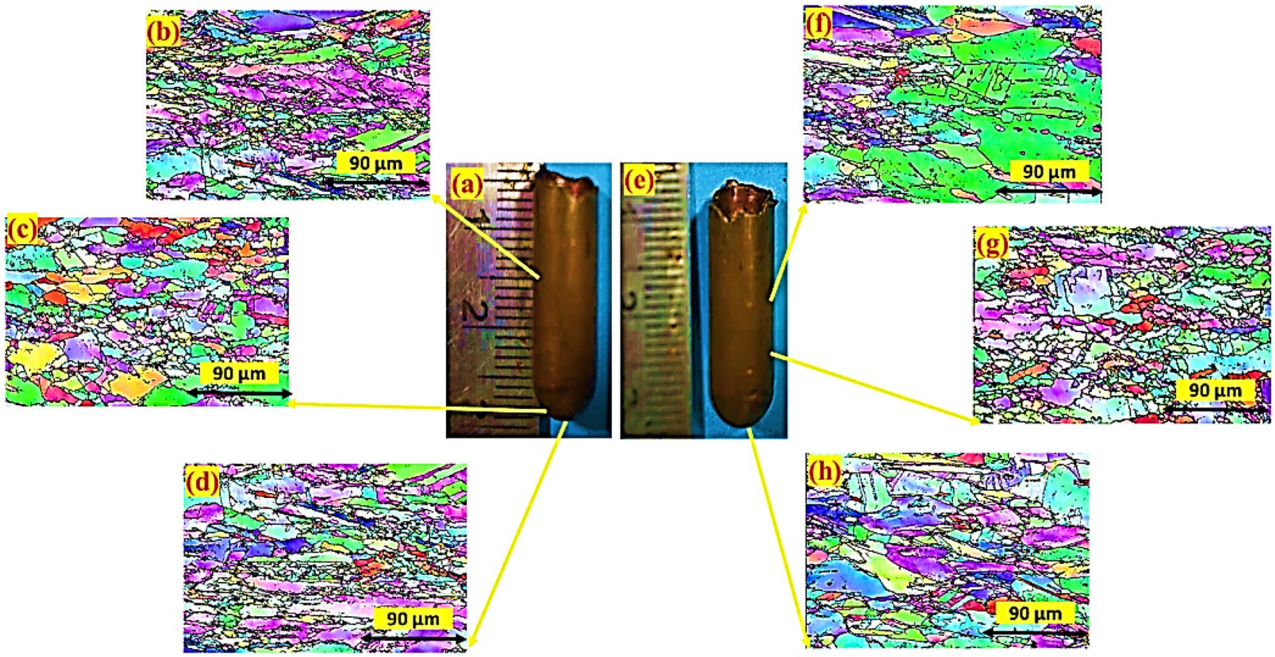

Fig. 13. Microstructural analysis of the fabricated cup; best condition, (**a**) Fabricated cup, (**b**) Wall thickness, (**c**) Cup nose radius, (**d**) Cup base, worse conditions, (**e**) Fabricated cup, (**f**) Wall thickness, (**g**) Cup nose radius, (**h**) Cup base.

Condition	Ra (µm)	DA (%)	WT (mm)	SB (µ)	Cup wall	Cup base	Cup radius	Overall performance
Best	0.28	98.5	0.32	2.1	Uniform & consistent	Smooth & accurate	Minimal deformation	Best - Minimal defects & stable shape
Worst	0.47	92.3	0.26	4.8	Uneven & thinner	Rough & less accurate	Uneven & thinner	Rough & less accurate

Table 10. Surface roughness (Ra) measurement.

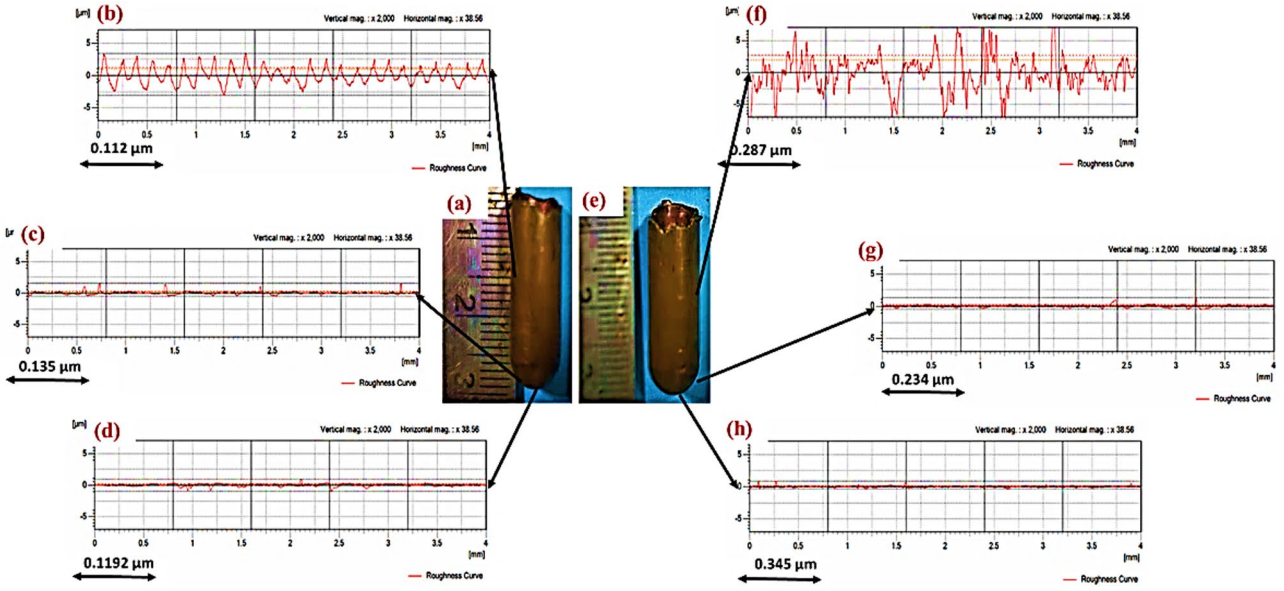

Fig. 14. Surface roughness fabricated cup best condition, (**a**) Fabricated cup, (**b**) Wall thickness, (**c**) Cup nose radius, (**d**) Cup base, worse conditions, (**e**) Fabricated cup, (**f**) Wall thickness, (**g**) Cup nose radius, (**h**) Cup base.

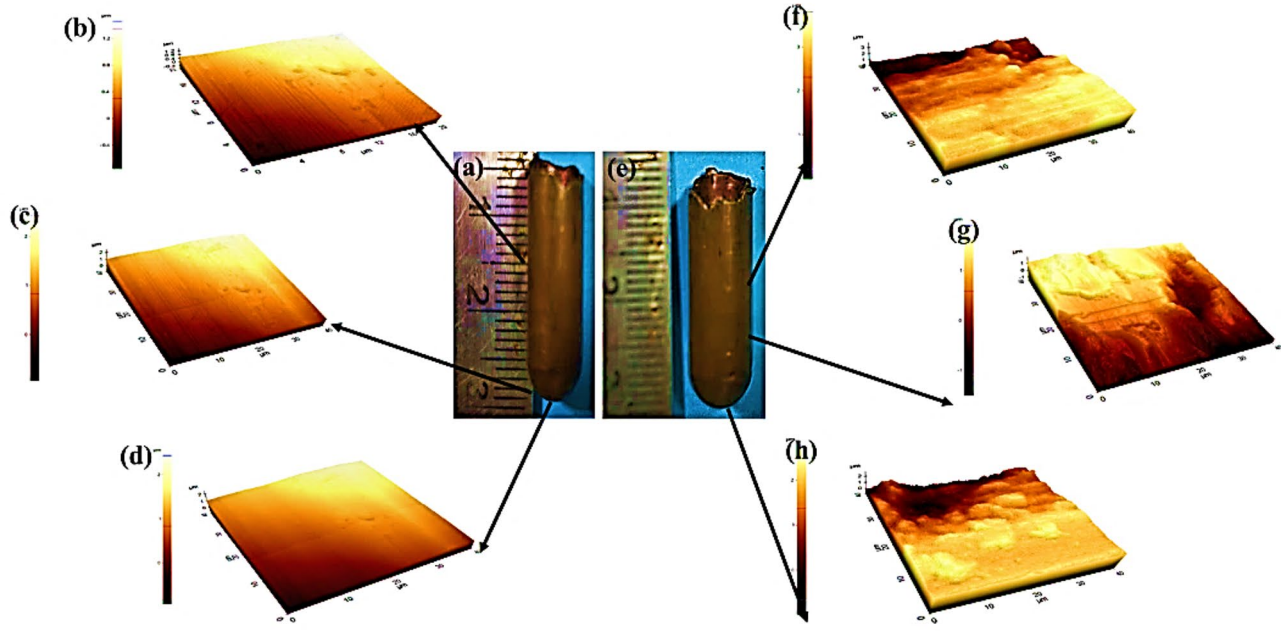

Fig. 15. Surface topography fabricated cup, best condition, (**a**) Fabricated cup, (**b**) Wall thickness, (**c**) Cup nose radius, (**d**) Cup base, worse conditions, (**e**) Fabricated cup, (**f**) Wall thickness, (**g**) Cup nose radius, (**h**) Cup base.

Condition	Base diameter (mm)	Wall height (mm)	Corner radius (mm)	Wall thickness (mm)	Total deviation (mm)	Accuracy status
Best case	1.859	4.601	0.199	0.188	0.004	High accuracy
Worst case	1.823	4.471	0.231	0.173	0.134	Poor accuracy

Table 11. Dimensional accuracy.

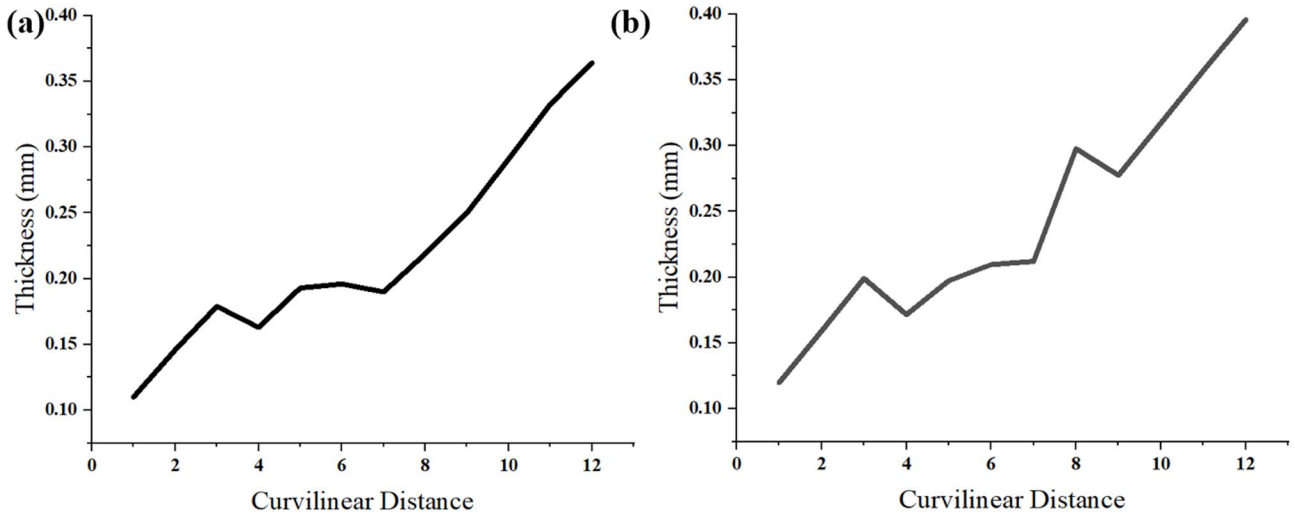

Fig. 16. Dimensional accuracy of fabricated cup; (**a**) Best, (**b**) Worse conditions.

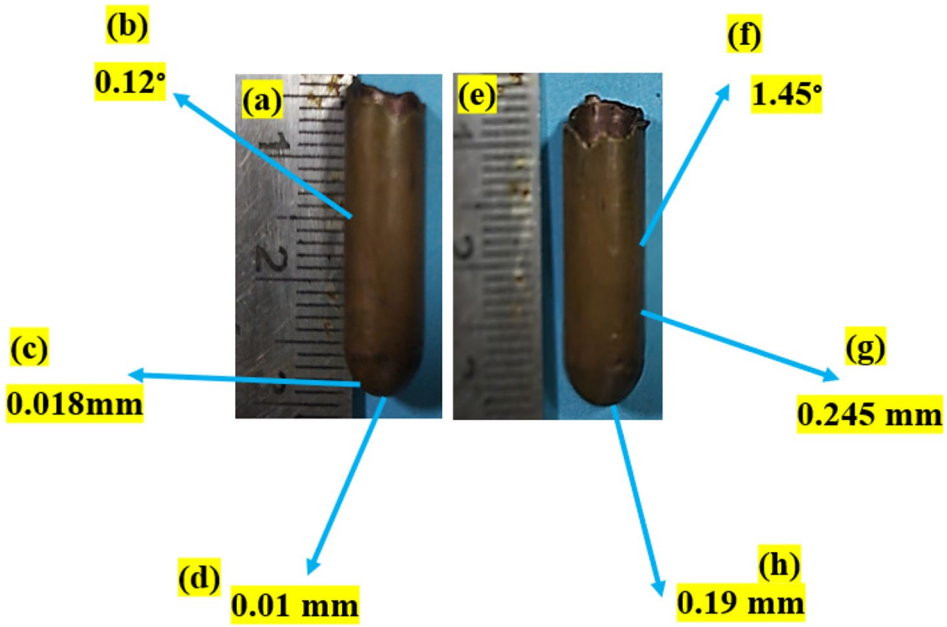

Fig. 17. Springback measurement of the fabricated cup; (**a**) Worse, (**b**) Best conditions.

Model significant

The ANOVA analysis confirmed that the selected input parameters—Clearance, Punch Radius, Draw Ratio, and Dry Lubricants—significantly influenced all response variables: RTF, SB, FLC, and MTR, with model p-values < 0.05. Among these, Dry Lubricants had the most consistent and significant effect across all responses, highlighting the critical role of tribological behavior in micro-deep drawing in Table 12. The lack-of-fit tests for all responses were not significant ($p > 0.05$), confirming the model's adequacy. Interactions such as AB (Clearance × Punch Radius) and AD (Clearance × Lubricant) also contributed notably, supporting the need for multivariable optimization strategies. These findings demonstrate that process parameters and lubrication

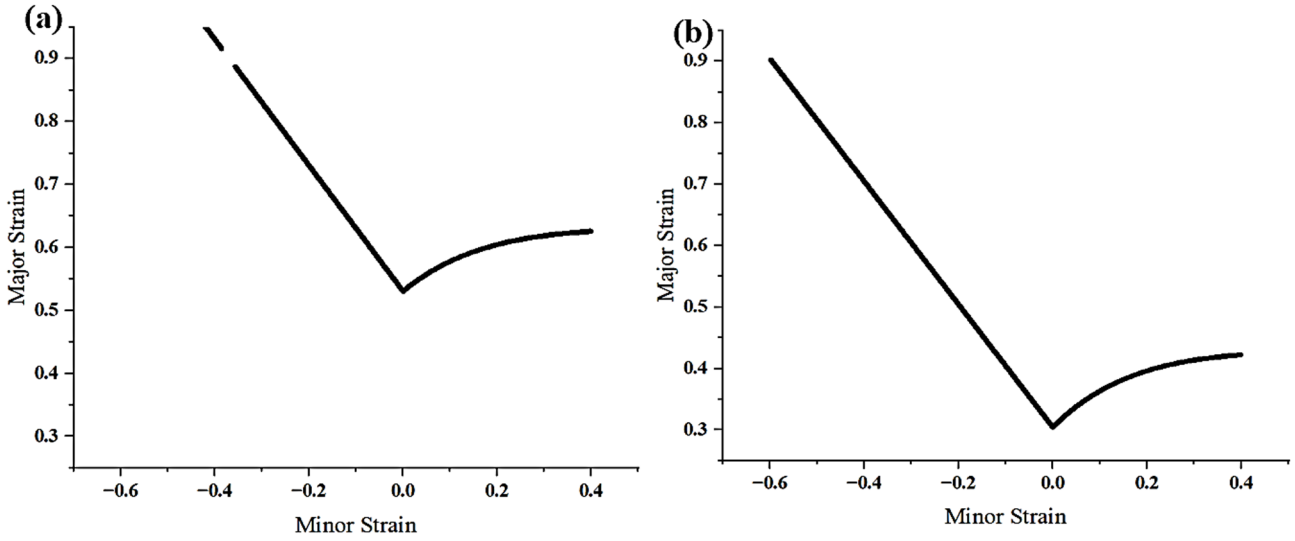

Fig. 18. Forming limit curve of fabricated cup; (**a**) Best, (**b**) Worse conditions.

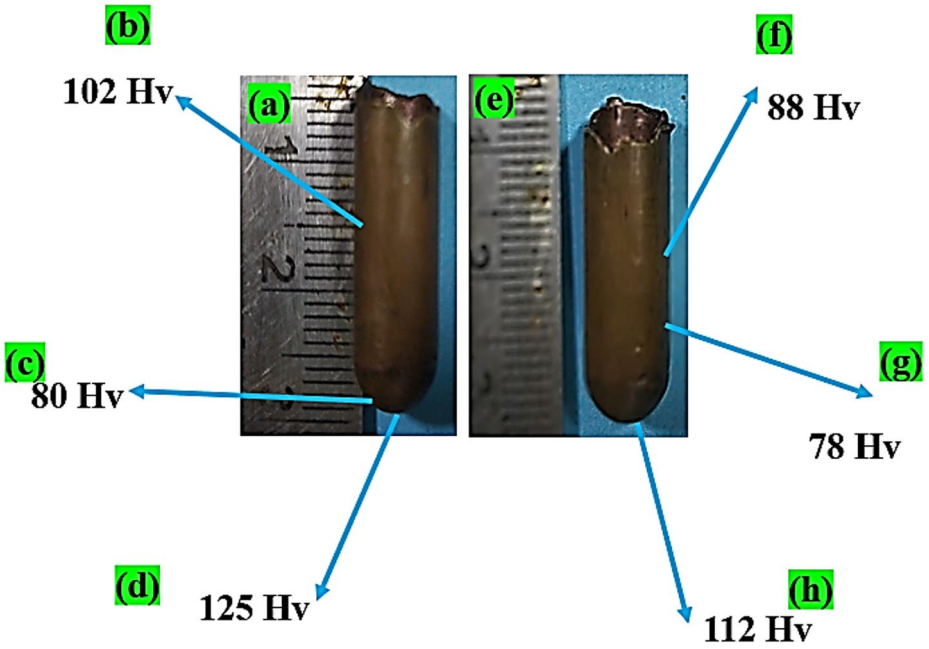

Fig. 19. Hardness test of fabricated cup; (**a**) Best, (**e**) Worse conditions.

selection are vital for improving dimensional accuracy and formability in micro-deep drawing. Though limited by a small experimental dataset, this study successfully correlated simulation predictions with experimental validations, confirming the reliability of the FEA-assisted Intuitionistic Fuzzy MARCOS optimization. Overall, the integrated modeling and experimental validation approach ensures high-precision process design in micro-manufacturing.

Goodness-of-fit metrics

The Key indicators, such as R^2 (coefficient of determination), were calculated to evaluate the predictive accuracy of the model. High R^2 values indicated strong model reliability. The model performance analysis reveals strong predictive capability across all output responses, as indicated by high R^2 values: 0.98 for RTF, 0.986 for SB, 0.978 for FLC, and 0.969 for MTR in Table 13. These values suggest that the developed regression models can explain over 96% of the variability in the experimental data, confirming high reliability. The adjusted and predicted R^2 values closely align with the R^2 values, indicating model stability and minimal overfitting. Additionally, low PRESS (Prediction Error Sum of Squares) and − 2 Log Likelihood values further validate the model's accuracy and goodness of fit. The coefficients of variation (C.V.%) for all parameters are within acceptable limits, signifying

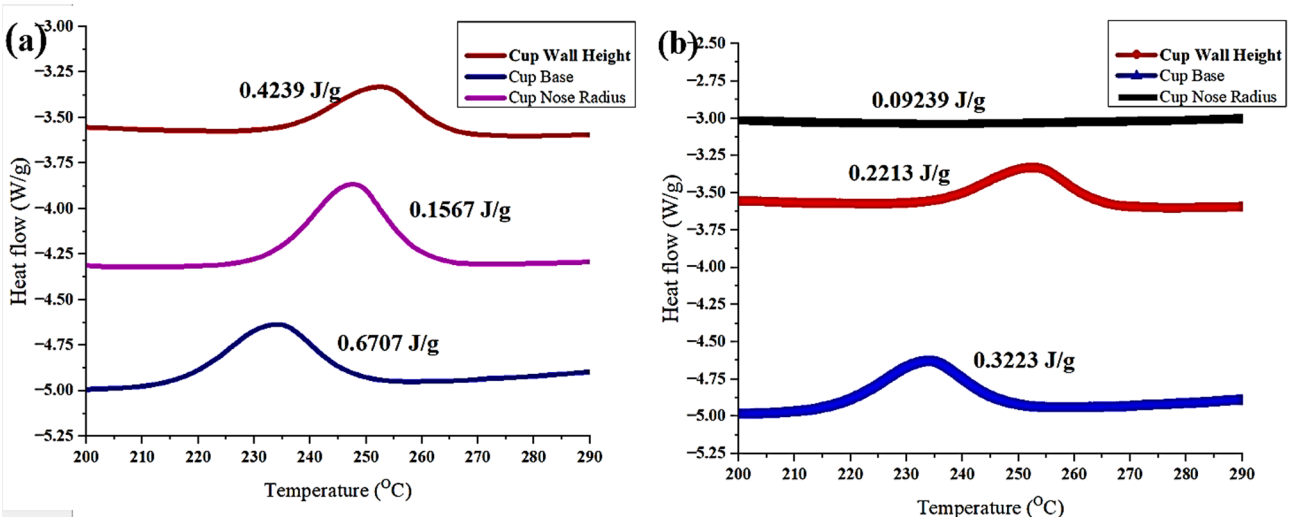

Fig. 20. DSC of fabricated cup; (**a**) Worse, (**b**) Best conditions.

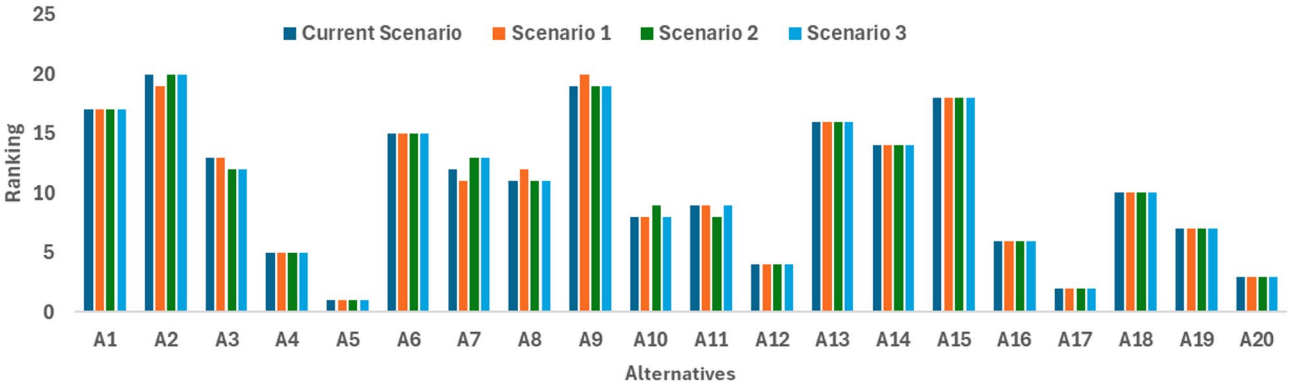

Fig. 21. Sensitivity analysis with different mesh sizes.

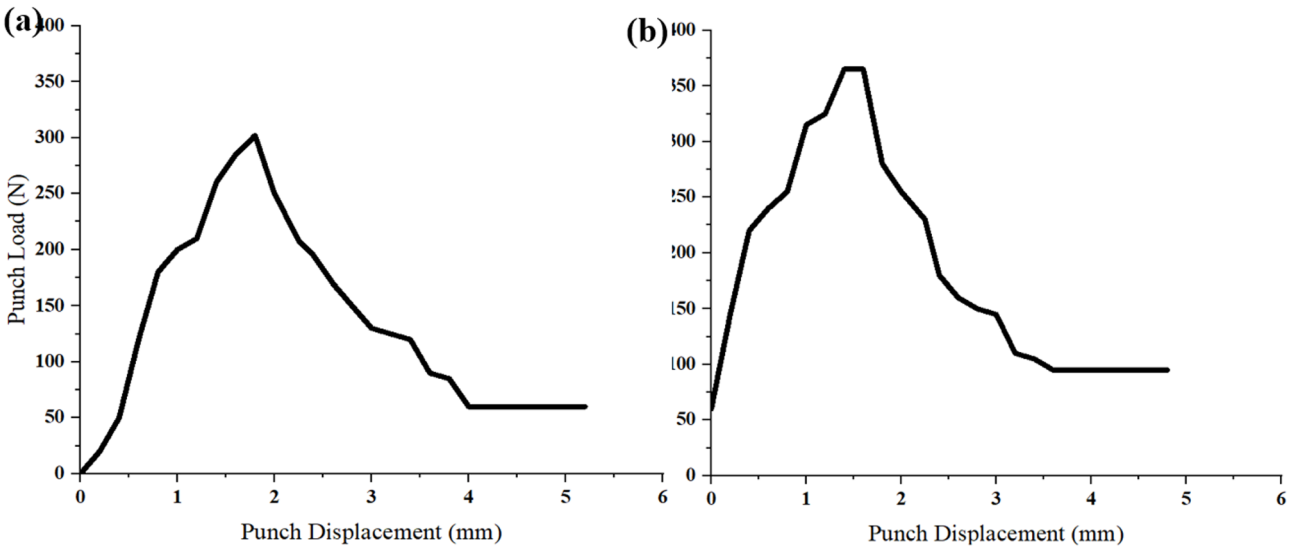

Fig. 22. Force- displacement of fabricated cup; (**a**) Worse, (**b**) Best conditions.

Source	Sum of squares				df	F value				Prob > F				Remarks
	RTF (N)	SB (µm)	FLC (%)	MTR		RTF (N)	SB (µm)	FLC (%)	MTR	RTF (N)	SB (µm)	FLC (%)	MTR	
Model	284.02	213.66	115.16	188.11	14	0.86	1.33	0.77	1.11	0.06	0.05	0.07	0.05	
A-clearance	4.82	0.02	2.90	4.29	1	0.21	0.00	0.27	0.36	0.07	0.10	0.06	0.06	
B-punch radius	18.48	2.26	22.65	2.34	1	0.79	0.20	2.12	0.19	0.04	0.07	0.02	0.07	
C-draw ratio	12.23	0.59	10.97	2.84	1	0.52	0.05	1.02	0.24	0.05	0.08	0.04	0.07	
D-dry lubricants	93.21	43.40	26.53	37.99	2	1.99	1.88	1.24	1.58	0.03	0.03	0.04	0.03	
AB	28.76	0.94	10.58	0.90	1	1.23	0.08	0.99	0.07	0.03	0.08	0.04	0.08	Significant
AC	22.40	0.00	8.28	0.02	1	0.95	0.00	0.77	0.00	0.04	0.10	0.04	0.10	
AD	27.06	0.14	11.44	1.16	2	0.58	0.01	0.53	0.05	0.06	0.10	0.06	0.10	
BC	0.83	6.27	3.34	5.14	1	0.04	0.54	0.31	0.43	0.09	0.05	0.06	0.06	
BD	23.47	12.44	9.65	5.90	2	0.50	0.54	0.45	0.24	0.06	0.06	0.07	0.08	
CD	22.39	12.67	4.22	17.24	2	0.48	0.55	0.20	0.72	0.07	0.06	0.08	0.06	
Residual	70.40	34.54	32.11	36.16	3									
Lack of fit	0.78	26.25	0.26	22.44	2	0.01	1.58	0.00	0.82	0.99	0.49	1.00	0.62	Not significant
Pure error	69.61	8.28	31.85	13.72	1									
Cor total	354.41	248.20	147.26	224.27	17									

Table 12. ANOVA.

Parameter	Std. Dev.	Mean	C.V. %	PRESS	-2 Log Likelihood	*R*-squared	Adj *R*-squared	Pred *R*-squared	Adeq precision
RTF (N)	4.844	13.701	35.357	577.91	75.629	0.98	0.941	0.937	3.17
SB (µm)	3.393	9.983	33.986	13709.4	62.812	0.986	0.921	0.902	4.808
FLC (%)	3.271	17.297	18.913	239.758	61.497	0.978	0.924	0.915	3.176
MTR	3.472	8.678	40.006	11732.59	63.637	9.839	0.969	0.956	3.868

Table 13. Model performance analysis.

Trail runs	Clearance, C	Punch radius, *R*	Draw ratio	Dry lubricants	RTF (*N*)		SB (µm)		FLC (%)		MTR		Remarks
					Simulation	Exp	Simulation	Exp	Simulation	Exp	Simulation	Exp	
2	0.475	1.5	1.69	MoS2	12.931	11.56	8.8404	9.678	16.100	15.567	8.736	8.56	Worse
5	0.285	1.5	1.69	Graphite	17.416	18.78	11.893	13.456	20.972	19.876	10.250	12.34	Best

Table 14. Validation of the optimized parameter.

consistent data dispersion relative to their means. Moreover, the Adequate Precision values for all responses exceed the threshold of 3.0, affirming an adequate signal-to-noise ratio. Collectively, these statistical indicators confirm the robustness, accuracy, and predictive strength of the models developed for simulating the responses.

Experimental confirmation

The experimental validation of the Intuitionistic Fuzzy MARCOS-based sustainable ranking of micro-cup production alternatives was carried out using directionally rolled copper rods. The press tool assembly consisted of a blank holder, punch, sheet metal, and lower die, forming the setup for micro-cup deep drawing operations. Different tool assemblies with systematically varied die–punch combinations were employed to replicate the ranked alternatives and assess forming behavior under diverse process conditions. Nakajima-type sheet metal samples were also tested to derive FLC, where the punch diameter was fixed at 6.5 mm and the die openings were gradually reduced to simulate different strain states. These experiments provided insights into formability and failure modes of copper rods under directional loading. Finally, the micro-cups produced (S1–S8) reflected clear variations in shape, size, and quality, confirming that the experimental outcomes closely matched the predicted rankings. This validates the proposed decision-making approach as an effective method for optimizing sustainable micro-forming parameters in high-precision manufacturing.

The optimized parameters derived from the Intuitionistic Fuzzy MARCOS approach were validated through real-time micro-deep drawing experiments in Table 14. Two representative trial runs (Trail 2 and Trail 5) were selected for comparison between FEA simulation and experimental outcomes across four key responses: RTF, SB, FLC, and MTR. Trial 5 exhibited closer alignment between simulated and experimental values, particularly in surface roughness and material deformation, indicating high fidelity of the simulation model. The deviations observed in Trial 2, such as higher experimental RTF and SB, suggest possible local frictional or material heterogeneities not fully captured by the simulation. These findings confirm that the FEA-based

optimization closely predicts real-world behavior, especially when supported by robust decision-making models like Intuitionistic Fuzzy MARCOS. Scientifically, this approach validates the significance of integrating multi-criteria decision-making with simulation for process optimization in microforming. The correlation between experimental and simulation data highlights the model's accuracy in predicting forming behavior, ensuring dimensional consistency and material integrity. Overall, the successful experimental validation confirms that the optimized parameters are effective for producing high-quality micro-cups with improved formability, dimensional accuracy, and minimal defects.

Conclusion

This study presents a comprehensive simulation-assisted process development approach for micro-deep drawing using the Intuitionistic Fuzzy MARCOS method, effectively balancing multiple objectives such as reduced tool force, controlled springback, improved formability, and minimal thinning. Key findings reveal that among the tested parameter combinations, the optimal configuration—Clearance of 0.285 mm, Punch Radius of 1.5 mm, Draw Ratio of 1.69, and Graphite lubricant—demonstrated superior mechanical and dimensional outcomes. ANOVA results confirmed the significance of main factors and interactions, while high R^2, adjusted R^2, and adequate precision values from Goodness-of-Fit metrics validated the model's predictive accuracy. The study highlights the importance of dry lubricant selection, with Graphite outperforming MoS_2 and PTFE in balancing force, formability, and thickness distribution. Experimental validation corroborated simulation predictions. Microstructural analysis, dimensional accuracy, wall thickness measurements, surface roughness, hardness, and DSC tests all aligned with simulation forecasts, reinforcing the model's reliability. Particularly, the optimal condition (Trail 5) showed better structural uniformity, lower springback, and enhanced formability compared to the worst condition (Trail 2). Practically, this study offers industries a structured decision-making framework for optimizing micro-forming processes while reducing trial-and-error costs. It promotes sustainability by enhancing forming efficiency, minimizing waste, and improving product quality. However, limitations include the use of a fixed draw ratio range and specific material (recrystallized copper), which may restrict generalizability. Future research could expand material types, explore additional lubricants, and integrate in-situ sensing for real-time process correction. Overall, the study contributes significantly to the field of micro-manufacturing by merging advanced simulation with fuzzy optimization and real-time validation. The methodology enhances process control, reduces experimental costs, and ensures high-quality micropart production, laying a foundation for broader application in precision forming technologies.

Data availability

Data is provided within the manuscript.

Received: 4 October 2025; Accepted: 19 November 2025
Published online: 10 March 2026

References

1. Anand, D. & Ravi Kumar, D. Effect of sheet thickness and grain size on forming limit diagrams of thin brass sheets. *Adv. Intell. Syst. Comput.* **757**, 435–444. https://doi.org/10.1007/978-981-13-1966-2_39 (2019).
2. Anwekar, S. Determination of strain distribution in single stage deep drawing process by finite element simulation. *IOSR J. Mech. Civil Eng.* **4** (5), 15–22. https://doi.org/10.9790/1684-0451522 (2012).
3. Bandyopadhyay, K. et al. Limiting drawing ratio and deep drawing behavior of dual phase steel tailor welded blanks: FE simulation and experimental validation. *J. Mater. Process. Technol.* **217**, 48–64. https://doi.org/10.1016/j.jmatprotec.2014.10.022 (2015).
4. Atul, S. & Babu, M. C. L. T. A review on effect of thinning, wrinkling and spring-back on deep drawing process. In *Proceedings of the Institution of Mechanical Engineers, Part B: Journal of Engineering Manufacture*. 1011–1036. https://doi.org/10.1177/0954405417752509 (SAGE Publications Ltd, 2019).
5. Behrens, G. et al. Influence of tool geometry variations on the limiting drawing ratio in micro deep drawing. *Int.J. Mater. Form.* **9** (2), 253–258. https://doi.org/10.1007/s12289-015-1228-9 (2016).
6. Banabic, D. et al. *Advanced Models for the Prediction of Forming Limit Curves*. 205–300. https://doi.org/10.1007/978-3-319-44070-5_5 (2016).
7. Ghassemali, E. et al. Effect of cold-work on the Hall-Petch breakdown in copper based micro-components. *Mech. Mater.* **80(Part A)**, 124–135. https://doi.org/10.1016/j.mechmat.2014.10.003 (2015).
8. Engel, U. & Eckstein, R. Microforming - From basic research to its realization. *J. Mater. Process. Technol.* 125–126. https://doi.org/10.1016/S0924-0136(02)00415-6 (2002).
9. Ma, J. et al. Microdeep drawing of C1100 microsquare cups using microforming technology. *Int. J. Adv. Manuf. Technol.* **82** (5–8), 1363–1369. https://doi.org/10.1007/s00170-015-7476-5 (2016).
10. Fu, M. W., Wang, J. L. & Korsunsky, A. M. A review of geometrical and microstructural size effects in micro-scale deformation processing of metallic alloy components. *Int. J. Mach. Tools Manuf.* **109**, 94–125. https://doi.org/10.1016/j.ijmachtools.2016.07.006 (2016).
11. Mevlut Fatih Peker. *Investigations on the Micro-Scale Surface Interactions At the Tool and Workpiece Interface in Micro-Manufacturing of Bipolar Plates for Proton Exchange Membrane Fuel Cells*' (2012).
12. Fu, M. W., Yang, B. & Chan, W. L. Experimental and simulation studies of micro blanking and deep drawing compound process using copper sheet. *J. Mater. Process. Technol.* **213** (1), 101–110. https://doi.org/10.1016/j.jmatprotec.2012.08.007 (2013).
13. Olguner, S. & Bozdana, A. T. The effect of friction coefficient on punch load and thickness reduction in deep drawing process. *Int. J. Mater.* **3**, 64–69 (2016).
14. Paradowski, B. et al. A sustainable approach for determining compromise ranking based on intuitonistic fuzzy score functions. In *Lecture Notes in Business Information Processing*. https://doi.org/10.1007/978-3-031-29570-6_10 (2023).
15. Saha, A. et al. A dual probabilistic linguistic MARCOS approach based on generalized Dombi operator for decision-making. *Iran. J. Fuzzy Syst.* **20** (2). https://doi.org/10.22111/ijfs.2023.7558 (2023).
16. Irthiea, I. K. *Process Analysis and Design in Micro Deep Drawing Utilizing a Flexible Die* (University of Glasgow, 2013).
17. Phanitwong, W. & Thipprakmas, S. Multi draw radius die design for increases in limiting drawing ratio. *Metals* **10** (7), 1–17. https://doi.org/10.3390/met10070870 (2020).

18. Lee, H. J. et al. Development of micro metal forming manufacturing system. *Mater. Sci. Forum* 505–507. https://doi.org/10.4028/www.scientific.net/msf.505-507.19 (2006).
19. Saeed, M. et al. Sustainable selection of microwave absorbing materials: A green evaluation under interval-valued intuitionistic fuzzy environment. *Clean. Mater.* https://doi.org/10.1016/j.clema.2024.100236 (2024). 11.
20. Salimian, S., Mousavi, S. M. & Antucheviciene, J. An interval-valued intuitionistic fuzzy model based on extended VIKOR and MARCOS for sustainable supplier selection in organ transplantation networks for healthcare devices. *Sustainability (Switzerland)* **14** (7). https://doi.org/10.3390/su14073795 (2022).
21. Takalkar, A. S. & Mailan Chinnapandi, L. B. Deep drawing process at the elevated temperature: A critical review and future research directions. *CIRP J. Manufact. Sci. Technol.* **27**, 56–67. https://doi.org/10.1016/j.cirpj.2019.08.002 (2019).
22. Vollertsen, F. et al. Size effects in manufacturing of metallic components. *CIRP Annals - Manuf. Technol.* **58** (2), 566–587. https://doi.org/10.1016/j.cirp.2009.09.002 (2009).
23. Takalkar, A. S. & Chinnapandi, L. B. M. Multi-stage deep drawing process of axis-symmetric extra deep drawing steel cylindrical cup. *Eng. Res. Express* **2** (2). https://doi.org/10.1088/2631-8695/ab872a (2020).
24. Yuan, S. et al. A novel deep drawing process for aluminum alloy sheets at cryogenic temperatures. *J. Mater. Process. Technol.* https://doi.org/10.1016/j.jmatprotec.2020.116743 (2020). 284.
25. Akkus, D. & Testik, O. M. A novel method for weighting decision makers for failure mode and effect analysis under intuitionistic fuzzy environment. *Qual. Reliab. Eng. Int.* **40** (4). https://doi.org/10.1002/qre.3510 (2024).
26. Aminzadeh, A., Parvizi, A. & Moradi, M. Multi-objective topology optimization of deep drawing dissimilar tailor laser welded blanks; experimental and finite element investigation. *Opt. Laser Technol.* **125** https://doi.org/10.1016/j.optlastec.2019.106029 (2020).
27. Chaurasiya, R. & Jain, D. Generalized intuitionistic fuzzy entropy on IF-MARCOS technique in multi-criteria decision making. In *Communications in Computer and Information Science*. https://doi.org/10.1007/978-3-030-81462-5_52 (2021).
28. Fan, J., Chai, M. & Wu, M. A new energy vehicle battery supplier selection using SWARA-MEREC-MARCOS approach under probabilistic triangular intuitionistic hesitant fuzzy environment. *J. Intell. Fuzzy Syst.* https://doi.org/10.3233/jifs-231975 (2024).
29. Hezam, I. M. et al. Standard deviation and rank sum-based MARCOS model under intuitionistic fuzzy information for hospital site selection. *Kybernetes* https://doi.org/10.1108/K-01-2023-0136 (2023).
30. Kizielewicz, B. et al. Towards the identification of MARCOS models based on intuitionistic fuzzy score functions. In *Proceedings of the 17th Conference on Computer Science and Intelligence Systems*. https://doi.org/10.15439/2022F249 (FedCSIS, 2022).
31. Mishra, A. R. et al. Assessment of battery energy storage systems using the intuitionistic fuzzy removal effects of criteria and the measurement of alternatives and ranking based on compromise solution method. *Energies* **15** (20). https://doi.org/10.3390/en15207782 (2022).
32. Bandyopadhyay, S. A novel multi-criteria decision analysis technique incorporating demanding essential characteristics of existing MCDA techniques. *Progress Artif. Intell.* **12** (3). https://doi.org/10.1007/s13748-023-00299-5 (2023).
33. Frini, A. A multicriteria intelligence aid methodology using MCDA, artificial intelligence, and fuzzy sets theory. *Math. Probl. Eng.* **2017** https://doi.org/10.1155/2017/9281321 (2017).
34. Ghajari, Y. E., Alesheikh, A. A., Modiri, M., Hosnavi, R. & Abbasi, M. Spatial modelling of urban physical vulnerability to explosion hazards using GIS and fuzzy MCDA. *Sustainability (Switzerland)* **9** (7). https://doi.org/10.3390/su9071274 (2017).
35. Gigović, L., Pamučar, D., Lukić, D. & Marković, S. GIS-Fuzzy DEMATEL MCDA model for the evaluation of the sites for ecotourism development: A case study of Dunavski ključ region, Serbia. *Land Use Policy* **58**. https://doi.org/10.1016/j.landusepol.2016.07.030 (2016).
36. Grabisch, M. & Labreuche, C. Fuzzy measures and integrals in MCDA. In *International Series in Operations Research and Management Science*. **233**. https://doi.org/10.1007/978-1-4939-3094-4_14 (2016).
37. Hamrani, A., Agarwal, A., Allouhi, A. & McDaniel, D. Applying machine learning to wire Arc additive manufacturing: a systematic data-driven literature review. *J. Intell. Manuf.* https://doi.org/10.1007/s10845-023-02171-8 (2023).
38. Indrajayanthan, V., Mohanty, N. K., Elavarasan, R. M. & Mihet-Popa, L. Investigation on current and prospective energy transition scenarios in Indian landscape using integrated SWOT-MCDA methodology. *Sustainability (Switzerland)* **14** (9). https://doi.org/10.3390/su14094940 (2022).
39. Kaymaz, Ç. K., Çakır, Ç., Birinci, S. & Kızılkan, Y. GIS-Fuzzy DEMATEL MCDA model in the evaluation of the areas for ecotourism development: A case study of Uzundere, Erzurum-Turkey. *Appl. Geogr.* **136**. https://doi.org/10.1016/j.apgeog.2021.102577 (2021).
40. Kumar, P., Sharma, R. & Bhaumik, S. MCDA techniques used in optimization of weights and ratings of DRASTIC model for groundwater vulnerability assessment. *Data Sci. Manage.* **5** (1). https://doi.org/10.1016/j.dsm.2022.03.004 (2022).
41. Ouma, Y. O., Yabann, C., Kirichu, M. & Tateishi, R. Optimization of urban highway bypass horizontal alignment: A methodological overview of intelligent Spatial MCDA approach using fuzzy AHP and GIS. *Adv. Civil Eng.* **2014** https://doi.org/10.1155/2014/182568 (2014).
42. Özkan, B., Sarıçiçek, İ. & Özceylan, E. Evaluation of landfill sites using GIS-based MCDA with hesitant fuzzy linguistic term sets. *Environ. Sci. Pollut. Res.* **27** (34). https://doi.org/10.1007/s11356-020-10128-0 (2020).
43. Papathanasiou, J. An example on the use and limitations of MCDA: the case of fuzzy VIKOR. *Examples Counterexamples* **1** https://doi.org/10.1016/j.exco.2020.100001 (2021).
44. Thakur, P. et al. A new entropy measurement for the analysis of uncertain data in MCDA problems using intuitionistic fuzzy sets and COPRAS method. *Axioms* **10** (4). https://doi.org/10.3390/axioms10040335 (2021).
45. Yatsalo, B., Korobov, A. & Martínez, L. From MCDA to fuzzy MCDA: violation of basic axiom and how to fix it. *Neural Comput. Appl.* **33** (5). https://doi.org/10.1007/s00521-020-05053-9 (2021).
46. Yatsalo, B., Radaev, A. & Martínez, L. From MCDA to fuzzy MCDA: presumption of model adequacy or is every fuzzification of an mCDA method justified? *Inf. Sci.* **587** https://doi.org/10.1016/j.ins.2021.12.051 (2022).
47. Ziemba, P. Selection of electric vehicles for the needs of sustainable transport under conditions of uncertainty—a comparative study on fuzzy Mcda methods. *Energies* **14** (22). https://doi.org/10.3390/en14227786 (2021).

Acknowledgements

We also wish to express our gratitude to Mr. Nilaalagan and Altair Inspire for providing the software used in this study. Additionally, other algorithms were implemented using Microsoft tools, generously made available to us by our university.

Author contributions

SSS: Conceptualization; Formal analysis; Investigation; Methodology; Resources; Software; Validation; Writing—original draft. SK: Conceptualization, Methodology, Investigation, Validation, Writing—review and editing. ATK: Conceptualization, Methodology, Investigation, Validation, Writing—review and editing.

Declarations

Competing interests
The authors declare no competing interests.

Additional information
Supplementary Information The online version contains supplementary material available at https://doi.org/10.1038/s41598-025-29817-2.

Correspondence and requests for materials should be addressed to T.K.A.

Reprints and permissions information is available at www.nature.com/reprints.

Publisher's note Springer Nature remains neutral with regard to jurisdictional claims in published maps and institutional affiliations.